970873

A Conceptual Model of DI Diesel Combustion Based on Laser-Sheet Imaging*

John E. Dec
Sandia National Laboratories

ABSTRACT*

A phenomenological description, or "conceptual model," of how direct-injection (DI) diesel combustion occurs has been derived from laser-sheet imaging and other recent optical data. To provide background, the most relevant of the recent imaging data of the author and co-workers are presented and discussed, as are the relationships between the various imaging measurements. Where appropriate, other supporting data from the literature is also discussed. Then, this combined information is summarized in a series of idealized schematics that depict the combustion process for a typical, modern-diesel-engine condition. The schematics incorporate virtually all of the information provided by our recent imaging data including: liquid- and vapor-fuel zones, fuel/air mixing, autoignition, reaction zones, and soot distributions. By combining all these elements, the schematics show the evolution of a reacting diesel fuel jet from the start of fuel injection up through the first part of the mixing-controlled burn (*i.e.* until the end of fuel injection). In addition, for a "developed" reacting diesel fuel jet during the mixing-controlled burn, the schematics explain the sequence of events that occurs as fuel moves from the injector downstream through the mixing, combustion, and emissions-formation processes. The conceptual model depicted in these schematics also gives insight into the most likely mechanisms for soot formation and destruction and NO formation during the portion of the DI diesel combustion event discussed.

INTRODUCTION

Diesel engine designers are challenged by the need to comply with ever more stringent emission standards while at the same time improving engine efficiency. In order to achieve these goals, a thorough understanding of the diesel combustion and emissions formation processes is critical.

One of the most fundamental elements of this understanding is a clear picture or "conceptual model" of how diesel combustion proceeds. An accurate conceptual model would provide a framework for interpreting experimental measurements, guide the development of numerical modeling, and furnish engine designers with a mental image to guide their thinking. Despite this need, the literature lacks an adequate description of how diesel combustion occurs.

Diesel combustion is a complex, turbulent, three-dimensional, multiphase process that occurs in a high-temperature and high-pressure environment. As a result, prior to the relatively recent advent of advanced laser diagnostics, detailed measurements of the events occurring within a reacting diesel fuel jet were not possible. Direct measurements consisted mainly of high-speed backlight, schlieren, and natural-flame-emission cinematography and sampling probe data. Although high-speed cinematographic data provide important information about the fuel-jet penetration and spread of the combustion zones, they have limited spatial resolution (integrated along the line of sight), are not species specific, and are not quantitative. More recently, sampling probes have provided some quantitative data, but they are perturbing, have poor temporal resolution, and do not give information about multiple points simultaneously, making the data hard to interpret. In addition, earlier data included combustion heat-release and fuel-injection rates that were derived from measurements of cylinder pressure and fuel-injector parameters, respectively; however, these data provide little detail about how the combustion process occurs.

Because information was limited and better measurements were not feasible, initial attempts to describe diesel combustion appear to have been adapted from studies of steady spray combustion in furnaces and gas turbines [1]. The quasi-steady portion of diesel combustion (after the starting transient up through the end of fuel injection) was thought to occur in a manner similar to other spray flames [1-3]. As discussed in detail in the Background section, this description showed the developed, reacting, diesel fuel jet as having a nearly pure-fuel core with diffusion-flame combustion occurring either around individual droplets or as a sheath around the jet periphery [3, 4]. Although many details were

* This work was performed at the Combustion Research Facility, Sandia National Laboratories and was supported by the U.S. Department of Energy, Defense Programs Technology Transfer Initiative and the Office of Transportation Technologies, and the Cummins Engine Company.

incomplete and/or unverified for diesel sprays, this description appeared to agree with most of the data from diesel combustion available at the time. Since it represented the best available attempt to draw a picture of the diesel combustion process, it was widely used by the diesel-engine community in discussions and was the basis of at least one diesel simulation model [5]. In addition to this description of the quasi-steady portion of diesel combustion, it was also widely thought that autoignition and the initial premixed burn occurred in regions where the equivalence ratio ranged from near the stoichiometric value up to about 1.5 [6-8].

More recently, the development of advanced laser-based diagnostics has provided a means for making detailed in-situ measurements of the processes occurring inside of a reacting diesel fuel jet. These diagnostics allow specific species within the reacting jet to be measured at multiple points simultaneously (planar imaging) with high spatial and temporal resolution, and many of these techniques can be designed to yield semi-quantitative and even fully quantitative data. Over the past eight years, laser diagnostics have been applied to direct-injection (DI) diesel combustion in a variety of optically accessible engines [9-20] as well as to "diesel-like" combustion in rapid compression machines [21-23] and diesel simulation vessels [24-28] that were also fitted with windows. These investigations have provided an abundance of new information on diesel combustion that, to a large extent, has not supported the earlier description of diesel combustion.

Among these recent investigations, those of the author and co-workers comprise perhaps the most complete data set. Using multiple laser-based planar imaging and natural-flame emission diagnostics in an optically accessible DI diesel engine of the heavy-duty size class, a variety of data on the diesel combustion and emissions formation processes have been obtained. These data include: liquid-phase fuel distributions [29, 30], quantitative vapor-fuel/air mixture images [30, 31], poly-aromatic hydrocarbon (PAH) distribution images, relative soot concentrations [13, 32-35], relative soot particle-size distributions [33-35], images of the diffusion flame structure [14], and natural-chemiluminescence images of the autoignition [34].

The combined results of these individual studies provide a detailed understanding of the temporal and spatial evolution of a reacting diesel fuel jet. This more complete understanding leads to a conceptual model of diesel combustion that explains all the data of the author and co-workers and concurs with the majority of other data in the literature. This new model differs significantly from the old description and offers new insight into the controlling physics of a combusting diesel fuel jet.

The objective of this paper is to present this conceptual model with appropriate supporting material in a self-contained form. Following this introduction is a background section that reviews selected literature describing the old picture of diesel combustion and presents some of our initial laser-sheet imaging data that first indicated an inconsistency with this picture. Next, our optically accessible diesel engine facility and operating conditions are described. This is followed by the main data presentation section which reviews previous investigations of the author and co-workers, reports new results on the onset of PAH formation and soot distributions under higher fuel load, and discusses these data with respect to other recent work in the literature. Then, the conceptual model of diesel combustion is presented as a series of idealized schematics and is contrasted with the old view. The paper ends with some concluding remarks in the last section.

BACKGROUND

OLD DESCRIPTION OF DIESEL COMBUSTION (PRIOR TO LASER-SHEET IMAGING)

In outward appearance diesel combustion is so complex that in a plenary lecture to the 20th Symposium (International) on Combustion in 1984, W. G. Agnew [1] described it as: *a "stew" in which liquid droplets of random sizes are squirted into a pot in an undefined spray to participate in a holocaust where nothing is homogeneous*. Perhaps because of this apparent complexity or perhaps because of the difficulty in conducting experiments under realistic diesel-engine conditions, initial attempts to describe diesel spray combustion did not arise from direct measurements of the diesel process. Rather, the description appears to have evolved from a combination of intuition and studies of spray combustion in furnaces and gas turbines, with the implicit assumption that the various spray combustion processes were closely related [1-3]. It should be noted that this description of spray combustion, derived from steady spray flames, was only intended to apply to the quasi-steady portion of diesel combustion after the starting transient (and premixed burn) and prior to the end of fuel injection, and that wall interactions were neglected [1, 2].

The basic concept of this description of spray combustion may be found in a paper by Faeth [2], and his schematic of a spray diffusion flame is reproduced in Fig. 1. As shown, the concept was zones of varying fuel-air mixture from center to edge of the spray. At the center was a cold very fuel-rich region, and the fuel concentration dropped off with a Gaussian-like profile toward the jet periphery. The combustion zone occurred at some distance from the center where the mixture was appropriate. The paper states that most measurements available at the time showed the disappearance of fuel droplets near the region of maximum temperature. However, it is not specific as to whether the combustion occurred as many separate small diffusion flames around individual droplets or as a single large diffusion flame sheath around the periphery of the spray, being fed by fuel vapor from many droplets. The inset in Fig. 1 appears to indicate a flame sheet around a group of droplets, but the paper also gives considerable discussion to individual droplet combustion.

Subsequently, this issue was addressed by H. Chiu et al. [4] and others [3, 36] who defined regimes for "sheath" combustion or droplet combustion depending on a parameter "G" (the ratio of the heat exchange between the liquid and vapor phases to the heat of vaporization). These various combustion modes and an example of how they might relate to spray combustion are shown in Figs. 2 and 3, respectively. These

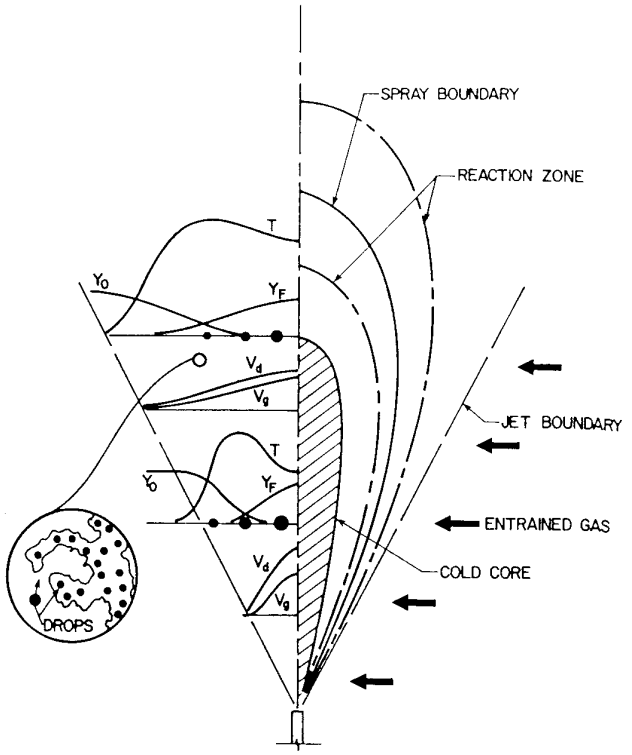

Figure 1. Reproduced from Faeth [2] with permission. Schematic representation of a coaxial spray diffusion flame.

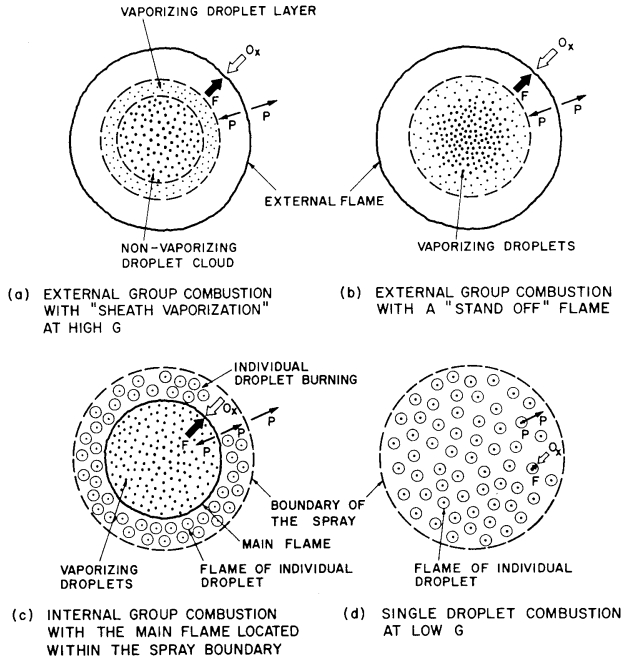

Figure 2. Reproduced from Kuo [3] with permission, as adapted from H. Chiu et al. [4]. Four group combustion modes of a droplet cloud.

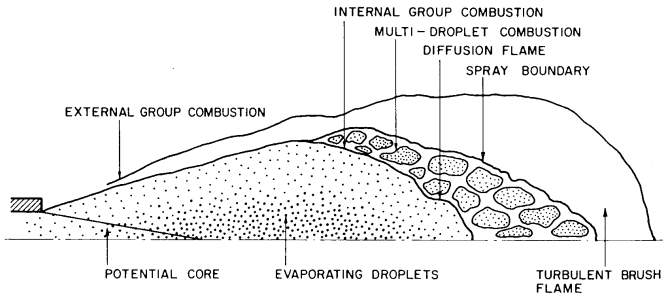

Figure 3. Reproduced from Kuo [3] with permission, as adapted from H. Chiu and Croke [37]. Schematic of group combustion for a liquid-fuel spray.

figures are reproduced from Kuo [3] who adapted them from the work of H. Chiu and co-workers [4, 37]. As described by Kuo [3], this theory was thought to be especially useful for dense sprays including those in diesel engines. Although the parameters put forth in these works suggest sheath-type combustion for diesel diffusion flames, this appears not to have been universally embraced by the diesel community. For example, the Bosch Automotive Handbook [8] discusses diesel mixture formation in terms of the regions around individual fuel droplets that contain a flammable mixture, implying that combustion occurs around the individual droplets.

Despite this lack of consensus as to the exact nature of the diffusion flame zone (a sheath flame, a collection of individual droplet flames, or some combination of the two), the general spray-combustion picture shown in Fig. 1 seemed logical for the quasi-steady portion of diesel combustion. It also appeared to fit most of the limited data available at the time. As a result, it was generally accepted by the diesel engine community as a working description of DI diesel combustion. As the best available description, it was widely applied in discussions and in the thinking of engine designers and researchers. Some examples from the literature include: Greeves et al. [7, 38] who presented a sketch similar to Fig. 1 to discuss potential sources for unburned hydrocarbon emissions from DI diesel engines; and W. Chiu et al. [5] who adapted this general description of spray combustion into a model for simulating DI diesel combustion, as reproduced in Fig. 4.

The spray-flame theory from which the original diesel combustion description was derived dealt mainly with fuel vaporization, mixing, and combustion zones, and it is not specific as to the location of the soot formation. Since soot formation results from fuel pyrolysis at temperatures above about 1300 K [39], mixing with the hot (1000 K) in-cylinder air is not sufficient to induce soot formation, and combustion heating is required. Therefore, during the quasi-steady portion of diesel combustion, it was generally assumed that soot would form on the fuel-rich side of the diffusion flame where the temperatures were sufficiently high. The initial premixed burn was not considered to be an important source of soot production since it was thought occur in regions that were nearly stoichiometric, primarily around the jet periphery [7, 8].

A general schematic of this old view of the quasi-steady portion of DI diesel combustion is presented in Fig. 5. It is important to realize that this schematic is intended only to capture the general concepts discussed above in a way that is representative of how they were often applied by the diesel

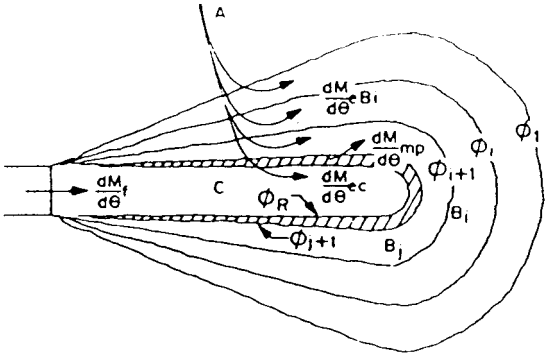

Figure 4. Reproduced from W. Chiu et al. [5], with permission. Schematic representation of combustion zones and entrainment rates for a transient spray mixing model of diesel combustion.

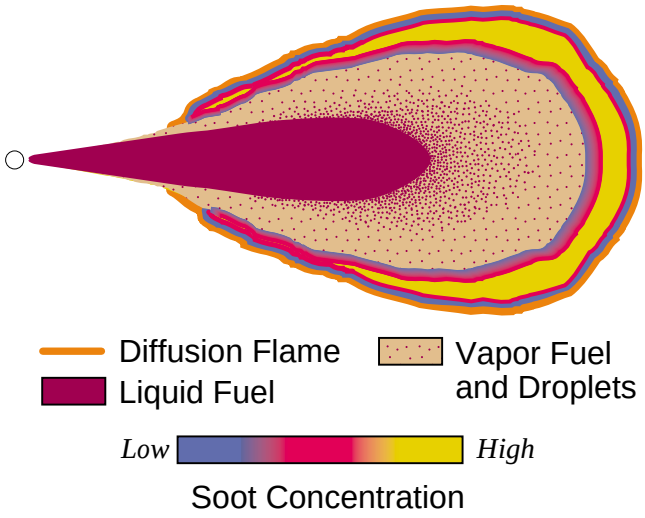

Figure 5. General schematic of the "old" view of diesel combustion (prior to laser-sheet imaging studies), showing a slice through the mid-plane of a reacting jet.

community. It cannot be exact, because this description was never developed to the level of a complete conceptual model of the type that will be presented later. This is because there was considerable uncertainty about the details, and because many of those who used this description recognized that it was not fully proven and that additional research was needed. In fact, some experimental data from sampling probes and high-quality shadowgraphs suggested that the picture of diesel combustion might be more complex [40, 41, 7], but these data were insufficient to provide a complete picture.

The schematic in Fig. 5 represents a slice through the mid plane of the combusting diesel fuel jet. The dark brown region depicts a region of dense fuel droplets (possibly with an intact liquid stream near the injector). This is surrounded by a region of more disperse, vaporizing droplets and vapor fuel (light brown). The diffusion flame (shown in orange) forms around the jet periphery where the fuel and air meet. In this schematic, considerable vapor-phase fuel is depicted prior to the flame zone, and the flame is shown as a continuous sheet as for the case of sheath-type combustion. Soot would then be expected to form around the jet periphery on the fuel-rich side of the reaction zone, as shown by the blue-red-yellow colors.

For the case of droplet combustion, significantly less fuel would be vaporized prior to the flame zone, and the flame zone would consist of numerous small flamelets surrounding individual droplets or clusters of droplets. In this case, soot formation would occur around each droplet (or droplet group) within the individual diffusion flamelets. However, interactions with the gas flow around the droplets could partially or completely extinguish the flamelets before soot burnout, resulting in a more homogeneous soot distribution around the jet periphery similar to that shown for the sheath flame case.

For either the sheath-flame or droplet-flame case, the old description of diesel combustion has three important characteristics. First, liquid-phase fuel penetrates well out from the injector with fuel droplets being present up to near (sheath-type) or within (droplet-flame) the combustion zone. Second, combustion occurs as a diffusion flame and is confined to the peripheral region of the jet. Third, soot occurs mainly in a shell-like region around the jet periphery.

EARLY LASER-SHEET IMAGING STUDIES

The development of laser-sheet imaging diagnostics and their application to DI diesel combustion offered, for the first time, direct detailed measurements of the diesel combustion process. Almost from the outset, these data indicated that the old description of diesel combustion might not be accurate, since soot was found in the central regions of the jet, well away from the periphery by the author and co-workers [12] and others [21, 24].

Shortly after these initial studies, the author applied simultaneous imaging of laser-induced incandescence (LII) and elastic-scattering to the downstream portion of a combusting diesel fuel jet to determine the distributions of liquid fuel, soot, and soot-particle size [33]. Pairs of these simultaneous images from two crank angles are reproduced in Fig. 6. These images were taken in a heavy-duty DI diesel research engine that was similar to our current engine (described in the next section), except that the optical access was more limited and a Cummins PT™ fuel injector was used. The circle around the images in Fig. 6 shows the view through the cylinder-head window which was similar to the one on our current engine but a little smaller (33.4 mm diameter). As with our current engine, the injector was located about 26 mm to the left of the field of view. The laser sheet was horizontal (13.1 mm below the cylinder head*), and it propagated from right to left. The fuel jet flowed from left to right at an angle 18° downward from horizontal, so the leading edge of the jet moved down through the plane of the laser sheet with increasing crank angle. The images were taken during the mixing controlled burn, prior to the end of fuel injection. A complete discussion of the details of this experimental setup may be found in Ref. [33].

* In Ref. [33] these data are reported as being in the 11.1 mm image plane. A 2 mm error in the positioning of the laser sheet was subsequently discovered and the correct image-plane location is reported here and in Ref. [32].

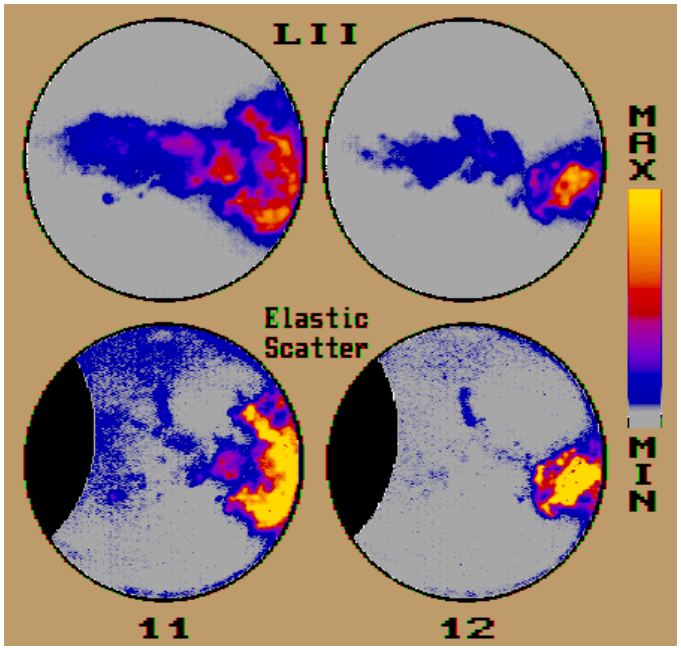

Figure 6. Adapted from Ref. [33]. Simultaneous LII (top) and elastic-scatter (bottom) images of a reacting diesel fuel jet in the plane 13.1 mm below the cylinder head. The crank angles ATDC, given at the bottom, were during the mixing-controlled burn, prior to the end of injection for this operating condition.

In Fig. 6, the LII images (top) show the spatial distribution of the relative soot concentration (volume fraction), since to first order the LII signal is proportional to the soot particle diameter to the third power [42-44]. The elastic-scatter images (bottom) show both soot and liquid-phase fuel, if it is present. For the soot, the elastic-scatter signal is proportional to the particle diameter to the sixth power [45] so the images will be biased to regions of larger particles. The signal intensity for both image types has been mapped to the blue-red-yellow false color scale shown at the right. Note that a portion of the elastic scatter images at the left hand edge has been blacked out because the horizontal laser sheet was hitting the top of the central cone on the "Mexican-hat" piston used in this experiment and creating an intense background scatter, see [33]. This noise does not occur in the LII images because the observed LII signal is spectrally shifted from the laser wavelength.

For each image pair, both diagnostics show a similar shape for the soot distribution in the head-vortex region toward the leading edge of the jet. However, the two image types are quite different upstream of the head vortex, where the LII images show soot throughout the jet while the elastic-scatter signal is very weak, barely distinguishable from the background noise except that it correlates spatially with the soot distributions in the simultaneous LII images.

Three important conclusions were drawn from a these images. First, soot is distributed throughout the cross section of the downstream portion of the reacting diesel fuel jet within the field of view. Second, there are no liquid fuel droplets within the field of view. If liquid fuel droplets were present, the elastic scatter signal would be very strong in the upstream portion (left and central part) of the lower images. This is because: a) liquid fuel originates at the injector and flows toward the leading edge of the jet, and b) elastic scattering is strongly dependent on particle size and liquid fuel droplets are typically much larger than the soot particles which give an easily detectable signal in the head vortex region. Third, based on the different sensitivities of LII (d^3) and elastic scattering (d^6) to particle size, these image pairs show that the soot particles in the upstream region are much smaller than those in the head vortex region. This finding, combined with the increase in soot concentration from the upstream region to the head vortex (seen in the LII images), suggests that the soot formation starts in the upstream portion of the field of view with formation and particle growth continuing as the soot moves down the jet toward the head vortex [33].

Although the early data set presented in Fig. 6 is far from a complete investigation of DI diesel combustion, these images clearly show a very different picture of the reacting diesel fuel jet than that expected from the old description (Fig. 5). Subsequent data have supported this new picture as will be shown in the following sections.

EXPERIMENT DESCRIPTION

OPTICAL-ACCESS ENGINE

The optical-access engine used in the studies described in the next section was a single-cylinder, direct-injection, 4-stroke diesel engine based on a Cummins N-series production engine. The N-series engine is typical of heavy-duty size-class diesel engines, with a bore of 140 mm and a stroke of 152 mm. These dimensions are retained in the optical-access engine, and a production Cummins N-series cylinder head is used so that the production engine intake port geometry is also preserved. The in-cylinder flow field of a similar Cummins N-series research engine has been examined under motored conditions and found to be nearly quiescent [46]. Figure 7 presents a schematic of the engine, and Table 1 summarizes its specifications.

The design of this engine utilizes a classic extended piston with piston-crown window. Additional windows located around the top of the cylinder wall provide the orthogonal optical access required for the two-dimensional (planar) laser imaging diagnostics. These windows allow the laser sheet to enter the cylinder along the axis of the fuel jet (see Fig. 7) or horizontally. A window in the cylinder head replaces one of the two exhaust valves to obtain a view of the squish region and the outer portion of the combustion bowl. Finally, this optical access engine incorporates a unique separating cylinder liner to allow rapid cleaning of the windows. A complete description of this engine may be found in Ref. [13].

This research engine is equipped with the Cummins CELECT™ electronic fuel injector. This closed-nozzle unit injector uses camshaft actuation to build injection pressures. A solenoid valve in the injector body controls the amount of fuel injected and the injection timing upon command from the laboratory computer. For the experiments presented here, the injector was equipped with an 8-hole tip. The hole

TABLE 1. Specifications of the Optical-Access Engine

Engine base type	Cummins N-14, DI Diesel
Cycle	4-stroke
Number of intake valves	2
Number of exhaust valves	1†
Intake Valve Opening	17° BTDC Exhaust‡
Intake Valve Opening	195° ATDC Exhaust‡
Exhaust Valve Opening	235° BTDC Exhaust‡
Exhaust Valve Closing	27° ATDC Exhaust‡
Bore	139.7 mm (5.5 in)
Stroke	152.4 mm (6.0 in)
Combustion chamber diameter	97.8 mm (3.85 in)
Displacement	2.34 liters (142 in^3)
Connecting rod length	304.8 mm (12.0 in)
Piston pin offset	None
Compression ratio	10:1 or 11:1 (See Table 4)

† In this optically accessible engine, one of the two exhaust valves of the production cylinder head was replaced by a window and periscope.

‡ All valve timings correspond to the crank angle when the valve first starts to move from fully closed.

diameter was 0.194 mm and the nominal angle of the fuel-jet axis was 14° downward from horizontal. Table 2 summarizes the specifications of the fuel injector. The injector is instrumented with a Hall-effect needle lift sensor, and injection pressure is determined from strain gage measurements of the force in the pushtube that activates the injector. Injection pressures and needle-lift data presented in this article are typical of those of N-series production engines using this injector at the operating conditions studied.

To minimize vibration, the engine was connected to a balancing box with counter-rotating balancing weights and mounted on a spring-mounted isolation pad. The engine was motored and its speed controlled by a 75 hp dynamometer. An air compressor supplied pressurized intake air that was dehumidified, highly filtered [30], and heated. The fuel, also highly filtered, was supplied by either a nitrogen-pressurized tank [30] or by a stainless steel diaphragm pump [14] to eliminate the small metal particles that can result from a gear-type pump.

TABLE 2. Specifications of the Fuel Injector

Type	Cummins CELECT™
Design	Closed-nozzle, unit injector
Number of holes	8, uniformly spaced
Hole diameter	0.194 mm
Length/diameter of holes (l/d)	4.1
Angle of fuel-jet axis (from horizontal)	14°

OPERATING CONDITIONS AND FUELS

All the data presented in the next section of this article were taken at an engine speed of 1200 rpm. Before conducting the experiments the engine was heated to 368 K (95° C) by means of electrical heaters on the "cooling" water and lubricating oil circulation systems. To minimize the rate of window fouling and to avoid overheating, the engine was

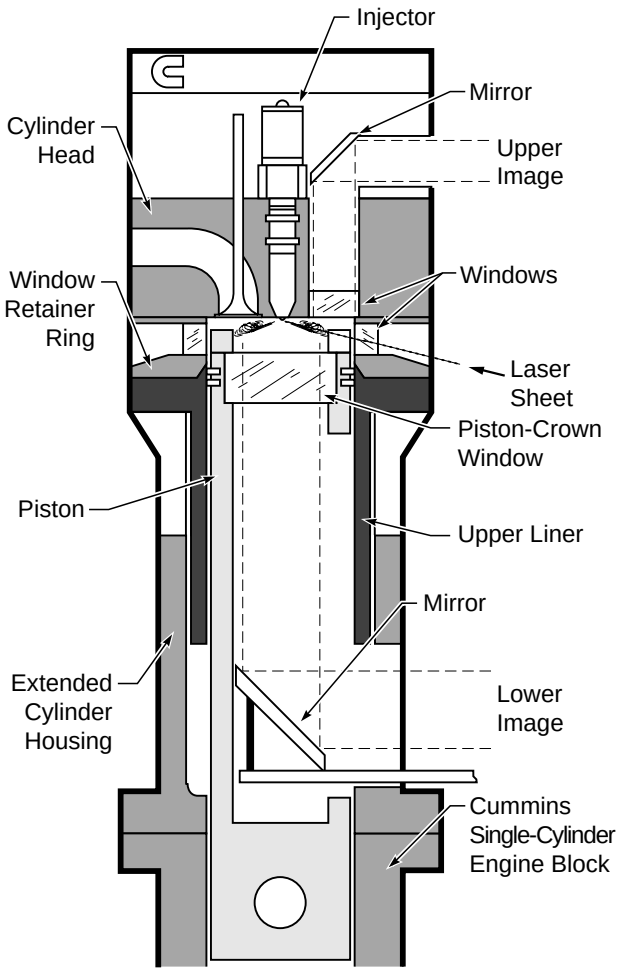

Figure 7. Schematic of optical-access diesel engine showing the laser sheet along the fuel jet axis. Images were obtained through both the cylinder-head window (upper image) and the piston-crown window (lower image). The upper liner is shown in the operating position.

fired once every 10th or 20th engine cycle, at which time the data were acquired.

Three fuels and two operating conditions were used for the studies summarized in this article. Because these fuels and operating conditions have been fully described in previous articles [13, 34, 35], they will only be briefly reviewed here. The fuels consisted of the following: 1) the "reference fuel," a 42.5 cetane number mixture of the diesel reference fuels (heptamethylnonane and *n*-hexadecane); 2) "low-sooting fuel #1," a mixture of 70% tetraethoxypropane and 30% heptamethylnonane by volume; and 3) "low-sooting fuel #2," a mixture of 80% 2-ethoxyethyl ether and 20% heptamethylnonane by volume. The low sooting fuels were required for some measurements to reduce the soot concentrations within the jet to permit the application of optical diagnostics. Low-sooting fuel #1 was selected so that the ignition delay at the base operating condition (discussed below) matched that of the 42.5 cetane number reference fuel. Low-sooting fuel #2 had a higher effective cetane number, so the intake air conditions were adjusted as discussed below to obtain the same ignition delay time as with the other two fuels. Despite this

drawback, low-sooting fuel #2 produced lower soot concentrations in the jet so it was used for imaging soot concentrations during the mixing controlled burn under higher load conditions. A basic assumption in using a low-sooting fuel for soot imaging is that the combustion process is mixing-rate limited, so that differences in the combustion chemistry with the low-sooting fuel change only the amount of soot formed and not its spatial or temporal distribution [32, 34]. Because the vaporization rate can affect mixing, care was taken to insure that the boiling points of the low-sooting fuel constituents were near those of the reference fuel and those of some representative diesel fuel constituents. These fuels are described in Table 3.

TABLE 3. Fuels

Reference Fuel	**67.6% heptamethylnonane and 32.4% *n*-hexadecane**
Cetane No.	42.5
Specific Gravity	0.7865
Fuel Injected per Cycle	0.0858 ml
Low-Sooting Fuel #1	**70% tetraethoxypropane and 30% heptamethylnonane**
Estimated Cetane No.	42.5
Specific Gravity	0.8812
Fuel Injected per Cycle	0.0960 ml†
Low-Sooting Fuel #2	**80% 2-ethoxyethyl ether and 20% heptamethylnonane**
Specific Gravity	0.8858
Fuel Injected per Cycle	0.1554 ml†
Boiling Points of Constituents (1 Atm.)	
2,2,4,4,6,8,8 Heptamethylnonane	240° C
n-Hexadecane	287° C
1,1,3,3 Tetraethoxypropane	220° C
2-Ethoxyethyl Ether	185° C

† Because the low-sooting fuels have a lower heating value than the reference fuel, additional fuel was supplied to give the same total apparent heat release.

A somewhat unique characteristic of the fuel injector used is that changing the amount of fuel injected (at an otherwise fixed operating condition) changes only the injection duration and not the initial injection rate. This means that the initial jet development and heat release rate are identical for either a low or high load condition up to the point that fuel injection ends. As a result, a relatively low fuel load (overall equivalence ratio of 0.25) could be used to minimize window fouling for most of the studies presented, which were concerned only with events up through the first part of the combustion process. A higher fuel loading (overall equivalence ratio 0.43) was used only for the soot studies later in the cycle. These fueling rates will be referred to as the low and high loads, respectively.

Most measurement were made using either the reference fuel or low-sooting fuel #1 at the low fuel load [34]. Because modifications required for optical access resulted in a compression ratio of only about 10:1 for these studies, intake air temperatures and pressures were increased to 433 K (160° C) and 206 kPa absolute to create realistic diesel-engine TDC (top dead center) conditions as listed in Table 4. It also produced a realistic ignition delay and premixed-burn fraction. These intake conditions will be referred to as the base operating condition.

A second operating condition was used for the high-load soot distribution studies. For these studies, the engine had a compression ratio of about 11:1 (as discussed below), and low-sooting fuel #2 was used which had a higher cetane number [13, 35]. The intake air conditions were set to 308 K (35° C) and 147 kPa absolute so that the ignition delay, magnitude of the premixed burn, and the TDC density were all similar to those obtained at the base condition. A higher peak injection pressure was reached for the high load because injection pressure continues to build during the increased injection duration. The operating conditions are summarized in Table 4.

DATA ACQUISITION AND OPTICAL SETUP

Figure 8 presents plots of the cylinder pressure, injector needle lift, and apparent heat release rates for the low- and high-load operating conditions. The data were digitized and recorded at half crank-angle-degree increments and ensemble-averaged over 20 engine cycles, and the procedure for computing the apparent heat release rates is discussed in Ref. [29]. For the low-load condition, only the plot of the reference fuel is presented (Fig. 8a) since the corresponding plot of low-sooting fuel #1 is virtually identical as shown in Ref. [34]. Note that, as indicated by the needle lift, the start of

TABLE 4. Engine Operating Conditions

Engine speed	1200 rpm
Water temperature	95° C
Oil temperature	95° C
Low Fuel Load	
Average equivalence ratio	0.25
Peak injection pressure	68 MPa
High Fuel Load	
Average equivalence ratio	0.43
Peak injection pressure	86 MPa
Base Operating Condition	
Fuels	Reference Fuel & Low-Sooting Fuel #1
Start of injection	11.5° BTDC
Compression ratio (approximate)	10:1
Intake air temperature	433 K (160° C)
Intake air pressure	206 kPa (absolute)
Motored TDC pressure	5.0 MPa
Estimated† motored TDC temperature	992 K
Estimated† motored TDC density	16.6 kg/m^3
High-Load Operating Condition	
Fuel	Low-Sooting Fuel #2
Start of injection	9.5° BTDC
Compression ratio (approximate)	11:1
Intake air temperature	308 K (35° C)
Intake air pressure	147 kPa (absolute)
Start of injection	9.5° BTDC
Motored TDC pressure	4.0 MPa
Estimated† motored TDC temperature	730 K
Estimated† motored TDC density	18.3 kg/m^3

† A polytropic coefficient of 1.36 was used to compute these estimates.

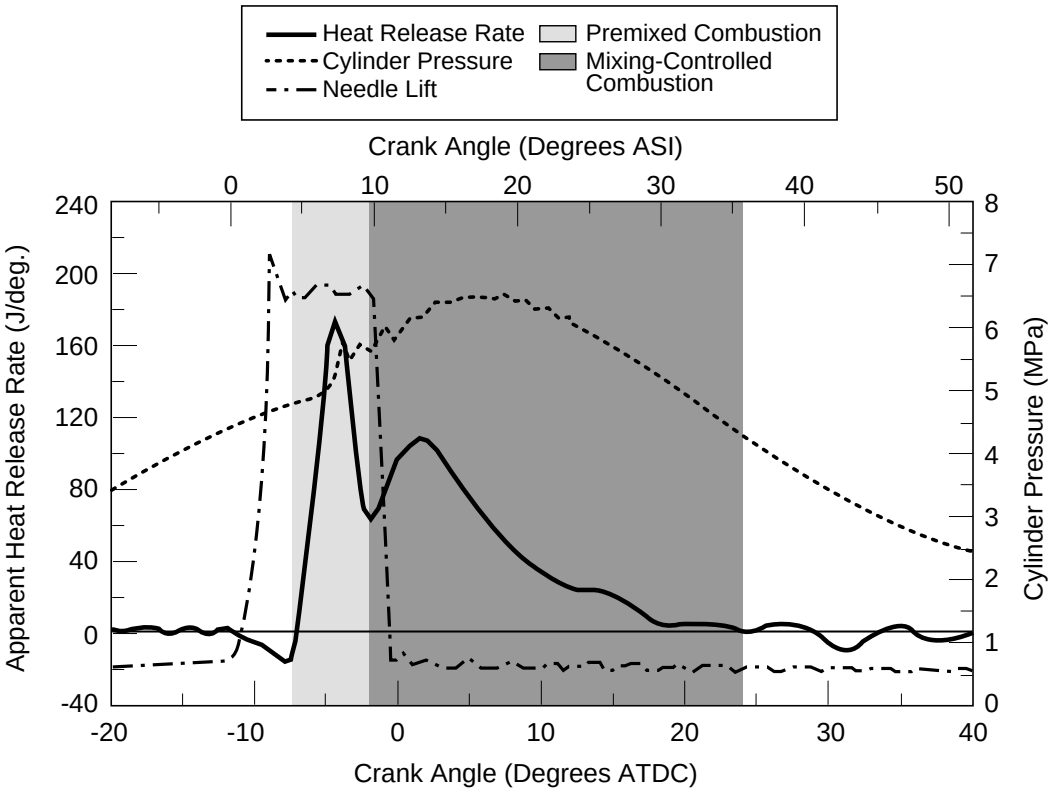

Figure 8a. Apparent heat release rate, cylinder pressure, and injector needle lift for the low fuel loading (ϕ=0.25) at the base operating condition (TDC temperature = 992 K, TDC density = 16.6 kg/m^3) using the reference fuel. The engine speed is 1200 rpm, and the data are ensemble-averaged over 20 cycles.

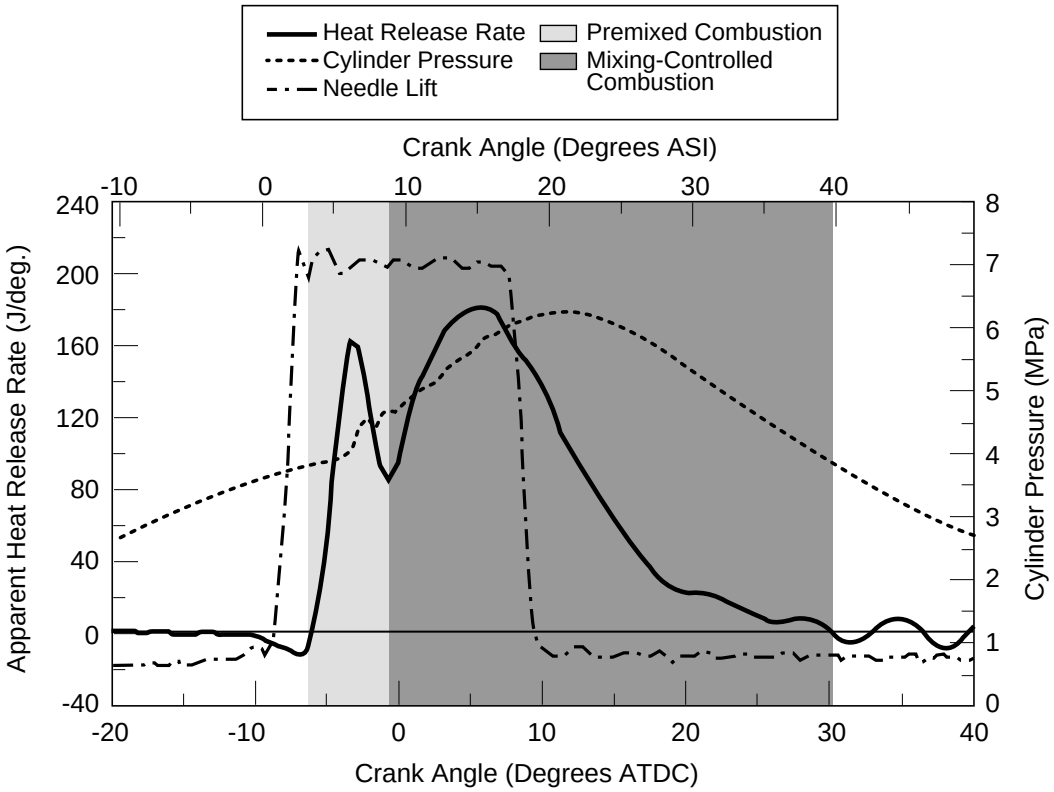

Figure 8b. Apparent heat release rate, cylinder pressure and needle lift for the high fuel loading (ϕ=0.43) at the high-fuel load conditions (TDC temperature = 730 K, TDC density = 18.3 kg/m^3) using the low-sooting fuel #2. The engine speed 1200 rpm, and the data are ensemble-averaged over 20 cycles.

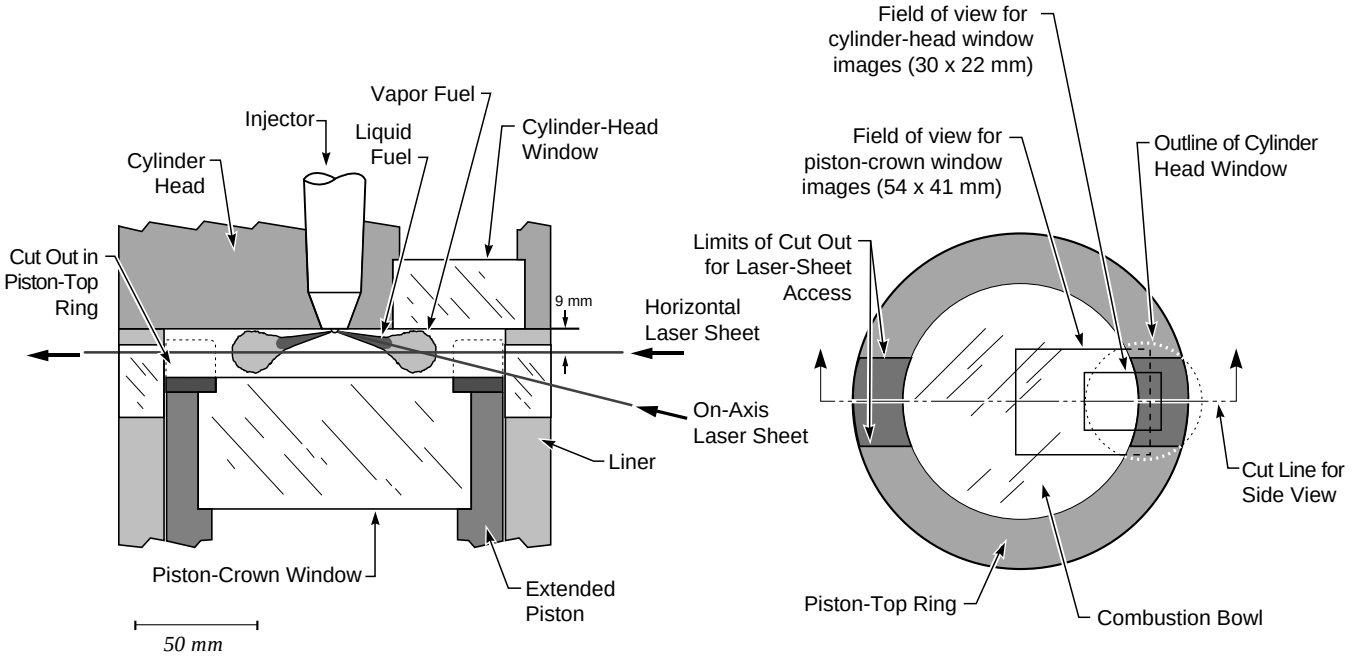

Figure 9. Geometry and optical configuration of the combustion chamber with cut outs in the rim for laser access. Figure 9a shows a side view of the combustion chamber and the two laser-sheet orientations. Figure 9b shows the top view of the piston and typical fields of view for images obtained through both piston-crown and the cylinder-head windows. The piston is shown at the TDC position.

injection was at 11.5° BTDC for the low load and 9.5° BTDC for the high load due to some changes in the fuel injector. This small difference is not thought to be significant since the piston motion is small near TDC. Because the time after the start of injection is the relevant parameter for the combustion process, all discussions in the remainder of this article will be given in crank angle degrees after the start of injection (ASI).

As is typically found in diesel combustion, the apparent heat release rate curves in Fig. 8 first go negative just after the start of injection as fuel vaporization cools the in-cylinder air. Then, after a few degrees, the combustion energy release exceeds that required for vaporizing the fuel, and the apparent heat release rises rapidly. The heat release rate curve then goes up through a local maximum and drops back down before rising again more slowly through a second local maximum. The initial sharp rise and fall is due to the rapid combustion of fuel that has premixed with air during the ignition delay period, and it is commonly referred to as the "premixed burn" or the "premixed burn spike". The second, broader hump in the curve is due to the mixing-controlled combustion and is commonly referred to as the "mixing-controlled burn".

Several different lasers, laser-sheet configurations, and camera setups were used for the various laser-sheet imaging data presented in this article. Only a general description will be given since the details may be found in the references. A frequency-doubled (532 nm) Nd:YAG laser was used for the LII and elastic scatter (liquid fuel, vapor fuel and soot) imaging. For the OH-radical and PAH fluorescence imaging, the doubled Nd:YAG pumped a dye laser whose output was either doubled (OH radical imaging at about 284 nm) or mixed with the residual fundamental of the Nd:YAG (PAH imaging at about 387 nm). The laser sheets were typically about 25 mm wide and 250 to 300 μm thick at the probe volume.

For all laser images, the laser sheet entered the combustion chamber through one of the windows at the top of the cylinder wall which was in line with one of the fuel jets. As shown in Fig. 9, the laser sheets were oriented either horizontally or along the fuel jet axis. The piston bowl rim was cut out in line with the laser sheet to permit the laser sheet to enter the combustion chamber near TDC. For some data sets where the horizontal laser sheet was used, the piston bowl rim was cut out on both sides of the combustion chamber, allowing the laser to exit the chamber to minimize back reflections (Fig. 9). The compression ratio was approximately 11:1 with a single cut-out in the bowl rim and 10:1 with cut-outs on both sides.

Images were acquired through both the piston-crown and cylinder-head windows with either one or two gated, intensified CCD video cameras. Various lens and filter combinations were used as appropriate. The image intensifier on the camera was calibrated [31] so that the intensities of images taken at different intensifier gain settings could be compared. For most data, the intensifier gatewidth was approximately 70 ns and the camera intensifier gate was synchronized with the 7 ns laser pulse. The camera had a video chip resolution of 380 by 480 pixels and was digitized by an 8-bit frame grabber in a personal computer to a resolution of 512 by 480 pixels.

Synchronization between the engine, laser, camera, and intensifier gate was controlled by a second personal computer and a digital delay generator, with the master signal coming from the engine shaft encoder. This synchronization system could be adjusted to obtain images at any desired crank angle within the half-degree resolution of the shaft encoder. Although each image has an effective exposure time of only about 7 ns, only one image could be acquired in a given cycle due to speed limitations of the laser and video recording system. Images were acquired in sets of 12 or 24, from 12 or 24 separate cycles. Each image presented has been subjectively selected as being representative of its respective set. The selected images are believed to be representative of their respective crank angles, and as such, they can be compared with the corresponding ensemble-averaged plots of the apparent heat release rate, cylinder pressure, and needle lift.

DATA PRESENTATION

This section presents images of various aspects of the diesel combustion process in the general order that they occur, from the start of injection to the end of the apparent heat release. Many of the image sets have been selected from previous works; others are original with this paper. The objective is to provide a comprehensive summary of our recent imaging data on DI diesel combustion and to discuss the relationships between the different measurements. These data form the basis for the conceptual model presented in the next section.

LIQUID-PHASE FUEL

Figure 10 shows a temporal sequence of liquid-phase fuel images reproduced from Ref. [29]. These images were obtained using the reference fuel with the low fuel load at the base operating condition, by elastic-scatter imaging through the piston crown window. A 532 nm narrow-band-pass filter isolated the elastically scattered light, and neutral density filters were used to attenuate the strong elastic (Mie) scatter signal from the liquid fuel droplets.

In each image, the location of the injector tip is evident at the center of the 8 fuel jets, and the gray curve at the right marks the edge of the combustion bowl (see Figs. 7 and 9). The horizontal distance from the injector to the edge of the combustion bowl is 49 mm, and the number at the upper right of each image gives the crank angle degree after the start of injection (ASI). The laser sheet enters the field of view from the right along the axis of the fuel jet in the 3 o'clock position. For these measurements, a laser-sheet thickness of 5 to 6 mm was used so that turbulent fluctuations did not move the tip of the liquid fuel out of the sheet. Initially all eight fuel jets are fairly well illuminated, and the liquid-fuel distribution between the jets appears uniform. Although a previous investigation [13] has shown that all eight fuel jets remain very symmetric throughout the combustion event, after about 2.0° ASI the jets do not appear uniform in Fig. 10 because the tips of most of the jets have traveled outside of the laser sheet and are no longer well illuminated. Only the fuel jet in the 3 o'clock position is well illuminated throughout the sequence,

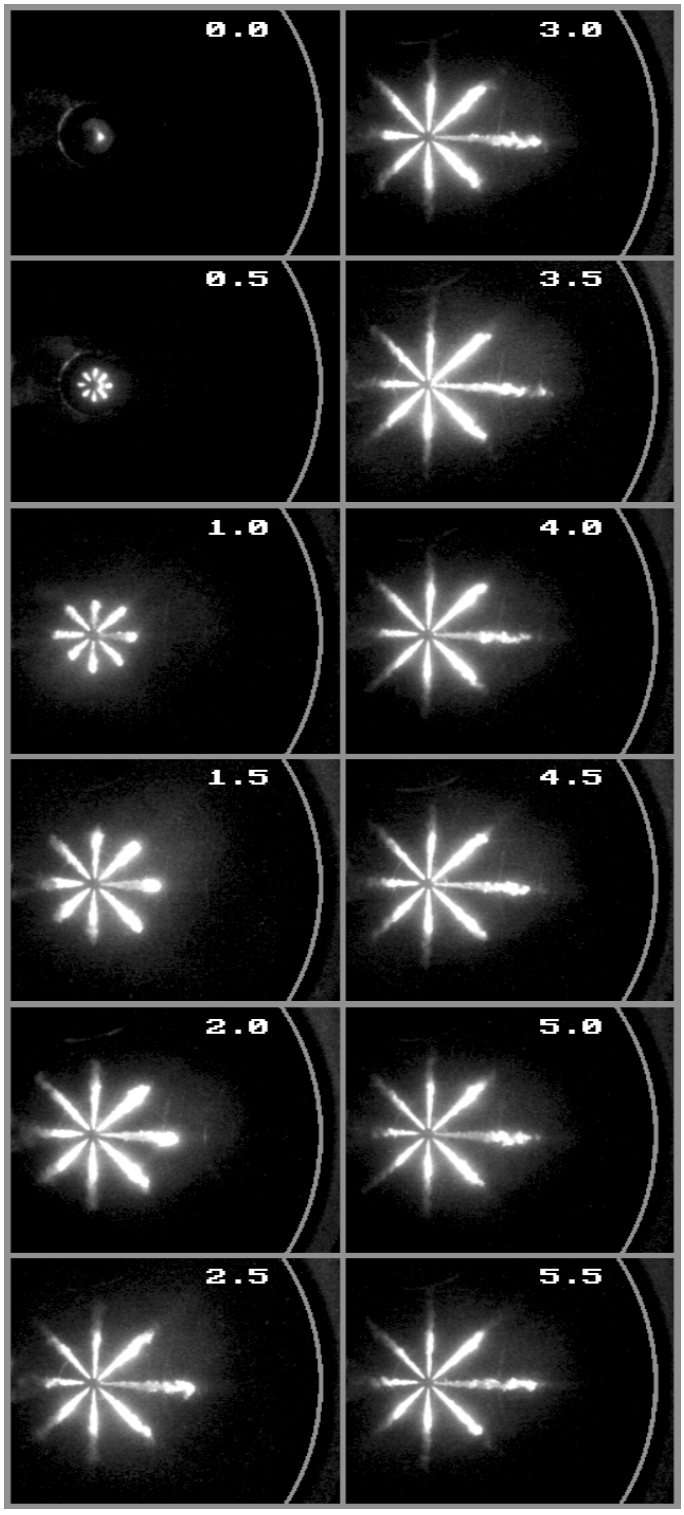

Figure 10. Reproduced from Espey and Dec [29]. Temporal sequence of elastic-scatter liquid-fuel images for base condition (TDC temperature = 992 K, TDC density = 16.6 kg/m^3). The crank angle degree ASI is given at the upper right of each image. The laser sheet propagates from right to left up the axis of the jet in the 3 o'clock position as shown in Fig. 9. All eight fuel jets are visible; however, only the jet in the 3 o'clock position is fully illuminated. The curve at the right of each image shows the edge of the combustion bowl. The horizontal distance from the injector to combustion bowl is about 49 mm.

and it is this jet which has been used to determine the liquid-fuel penetration length.

Following the image sequence in Fig. 10, it can be seen that fuel injection has not yet begun in the image labeled 0° ASI (-11.5° ATDC). This image corresponds to the timing of the start of first injector-needle motion. Injection actually starts sometime during the half-crank-angle degree (70 μs) interval between this image and the second image of the sequence which shows liquid fuel extending about 2.5 mm into the combustion chamber. Then, for the next 2.5 degrees, the extent of the liquid fuel increases rapidly reaching a length of about half the bowl radius (approximately 23 mm) by 3° ASI (-8.5 ATDC). Beyond 3° ASI, the liquid length remains fairly constant at about 23 mm, with a cycle-to-cycle variation of about ±2 mm [29].* Since Fig. 8a shows that the first indicated heat release does not begin until 4.0° ASI (-7.5° ATDC), a full crank-angle degree after the liquid fuel has reached its maximum length, the limited liquid-phase fuel penetration is not a result of combustion heating. It is due solely to the evaporation induced by entrainment of hot (heated by compression) ambient air into the fuel jet.

These results are in agreement with several other works in the literature that showed similar limited liquid-phase fuel lengths. In addition, these other works have also shown the effect of several parameters on the maximum liquid length. Espey and Dec [29] (the paper from which Fig. 10 is reproduced) showed that the maximum liquid length varied from 30 to 18 mm as the TDC temperature was increased from 800 to 1100 K at a constant density of 16.6 kg/m^3, and from 30 to 13 mm as the TDC density was increased from 11.1 kg/m^3 to 33.2 kg/m^3 at a constant temperature of 992 K. Kamimoto et al. [47] used backlight photography in a rapid compression machine to show that the limited liquid length was independent of injection pressure from 26 to 110 MPa. Browne et al. [48] used backlight photography to show that the liquid length increased as injector hole size increased (from 0.2 to 0.28 mm) and as the vapor pressure of the fuel decreased. The results of Bower and Foster [49], Bardsley et al. [9], Hodges et al. [18], and Baritaud et al. [19] also showed limited liquid-fuel lengths using an exciplex fluorescence technique.

Finally, it is important to realize that these liquid fuel images only show the presence of liquid fuel droplets and say nothing about what fraction of the fuel has vaporized. Thus, the abrupt end to the liquid phase (at about 23 mm for the base condition) is only the point where the last droplets vaporize. Vaporization undoubtedly begins much closer to the injector and continues progressively as the fuel moves down the jet until it is complete at the distance shown.

VAPOR-PHASE FUEL

Leading Region of the Jet - Although the liquid-phase fuel is completely vaporized within about 23 mm of the injector (for the base operating condition), vapor-phase fuel continues to penetrate across the chamber. Figure 11, reproduced from Ref. [31], shows quantitative planar laser Rayleigh scatter (PLRS) images of the vapor-fuel and air mixture in the region of the fuel jet just downstream of the maximum liquid-phase penetration (Fig. 9). These images were obtained through the cylinder-head window, and the left edge is located 26 mm horizontally (27 mm along the jet axis) downstream of the injector. The field of view is about 18.1 by 12.5 mm which is significantly magnified relative to the images in Fig. 10. The raw Rayleigh scatter images have been reduced to equivalence ratio fields as discussed in Ref. [31] and mapped to the false color scheme shown at the bottom of the figure. These images were taken with a horizontal laser sheet in the plane 9 mm below the cylinder head which is near the center of the vapor-fuel region, in the leading portion of the jet, for the crank angles examined (see Fig. 9). The horizontal laser-sheet orientation allowed the light to pass out of the cylinder on the opposite side of the combustion chamber, minimizing the background scatter. A 532 nm narrow-band-pass filter was used to isolate the PLRS signal.

Figure 11 shows the evolution of the vapor-fuel distribution for both reacting (left hand column) and non-reacting (right hand column) jets from 4.0° to 6.0° ASI. The reacting sequence was obtained using the reference fuel (cetane no. 42.5), while the non-reacting sequence was obtained using pure heptamethylnonane (cetane no. 15). As discussed fully in Ref. [31], the appearance of the fuel distributions in the reacting and non-reacting sequences is similar, up through 4.5° ASI. For both cases, at 4.5° ASI the equivalence ratio ranges generally from 2 to 4, and the edges of the jet along the sides and at the front are well defined by a sharp transition from the equivalence ratio levels within the jet down to the background. Only the outline of the turbulent jet differs due to cycle-to-cycle variation.

After 4.5° ASI (as the heat release rate curve begins its rapid rise, Fig. 8a), the sequences diverge significantly due to the effects of combustion in the reacting jet. From 4.5° to 5.0°, the equivalence ratio in the non-reacting jet (right) remains almost the same, while in the reacting jet (left) the PLRS signal intensity drops significantly throughout the cross section of the leading portion of the jet. As the sequence progresses, jet penetration and fuel/air mixing cause the equivalence ratio in the non-reacting jet to progressively decrease at a relatively slow rate, while in the reacting jet, the PLRS signal continues to decrease rapidly, so that by 6.0° ASI there are large regions with no significant signal. It should be noted that after 4.5° ASI, the images on the left are no longer quantitative, and the equivalence ratio mapping of the image intensity only serves as a method of comparing signal intensities with the other images.

As discussed in Ref. [31], the drop in the PLRS signal as the heat release begins can be caused by several effects, but an analysis of the data indicates that the initial large drop in PLRS signal from 4.5° to 5.0° ASI is mainly caused by fuel breakdown. Other factors such as conversion of fuel to products and local thermal expansion become more significant as combustion progresses and probably contribute to the eventual reduction of the signal to background levels.

* The region downstream of the maximum liquid penetration seen in Fig. 10 has been rigorously examined to prove that no liquid fuel droplets remain [30].

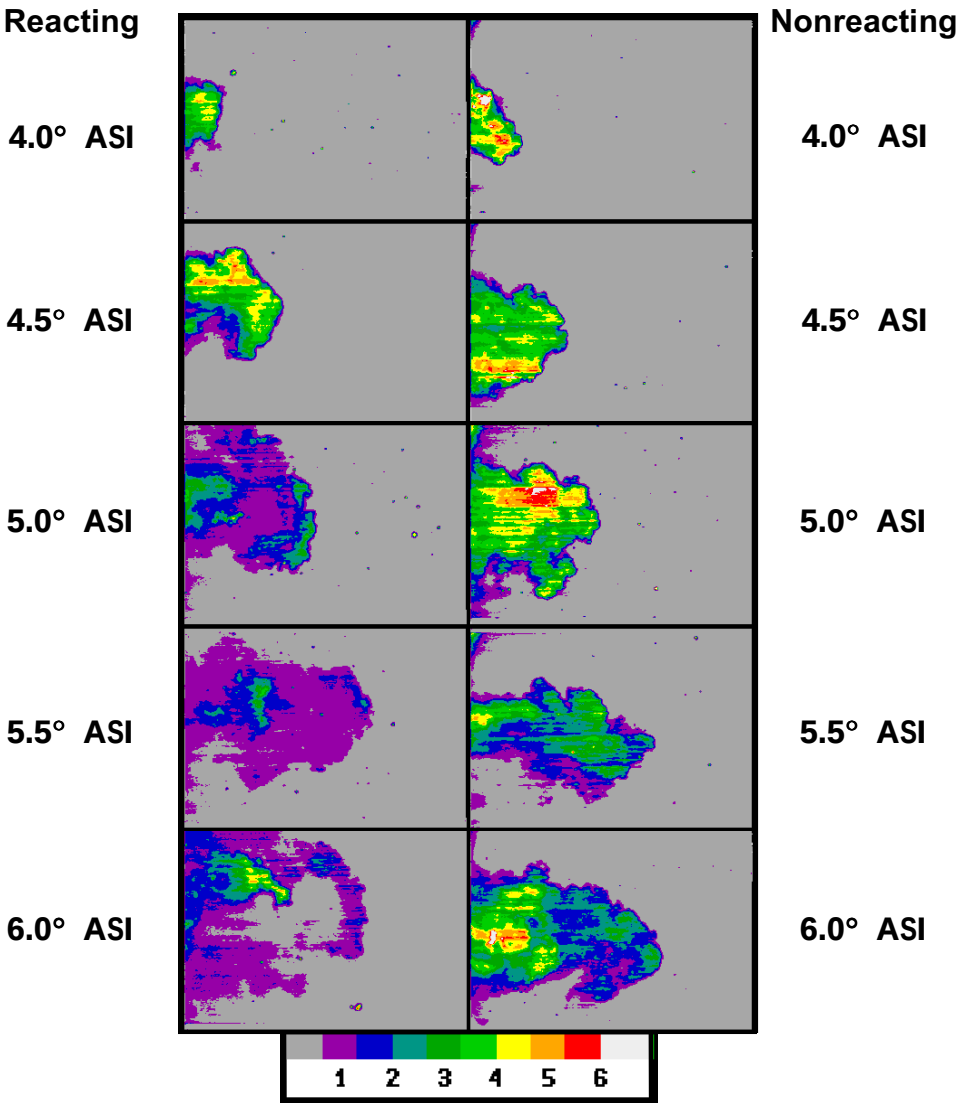

Figure 11. Reproduced from Espey et al. [31]. Temporal sequence of quantitative images of the equivalence ratio in the leading portion of the diesel fuel jet. The reacting jet (cetane no. = 42.5) is shown on the left, and the nonreacting jet (cetane no. = 15) is on the right. The crank angle degree after the start of injection (ASI) is given at the side of each image. The images were derived from PLRS images in the plane 9 mm below the cylinder head. The left edge of the image is 27 mm downstream of the injector nozzle, and the field of view is 18.1 mm by 12.5 mm. The equivalence ratios have been mapped to false colors as shown in the colorbar.

These vapor fuel images provide three significant new pieces of information about how diesel combustion occurs. First, they show that just downstream of the liquid-fuel region, the vapor-fuel and air are relatively well mixed to an equivalence ratio of 2 to 4. This fuel-rich but combustible mixture is present throughout the jet cross section; there are no regions of pure or almost pure fuel. Second, there is a sharp well-defined boundary separating this "relatively uniform" mixture from the surrounding air. A near-stoichiometric mixture occurs only in a very narrow region at the edges and therefore contains only a small fraction of the premixed fuel. Third, the breakdown of fuel throughout this fuel-rich premixed zone coincides with the initial rapid rise in the apparent heat release rate, indicating that the initial premixed burn is fuel-rich.

Along the Sides of the Liquid-Phase Fuel - The PLRS vapor-fuel images above show the vapor-phase fuel distribution in the leading region of the fuel jet, downstream of the maximum liquid-phase penetration. There is also strong evidence that a vapor-fuel region exists along the sides of the liquid-fuel distribution shown in Fig. 10, being extremely thin or non-existent near the injector and becoming progressively thicker downstream.

Hodges et al. [18] used exciplex fluorescence to examine liquid- and vapor-phase fuel distributions in a vaporizing diesel-like fuel jet. Their liquid phase images look qualitatively similar to those presented in Fig. 10.* Starting at a point about one-third of the way from the injector to the maximum liquid penetration length, their simultaneous vapor-phase fuel images show the vapor fuel along the sides of

* It is difficult to compare exact dimensions from the images of Hodges et al. [18] with those of the author and co-workers presented in this paper because the TDC temperature and density used by Hodges et al. were lower, and the vapor pressure of their fuel was higher than ours.

the liquid fuel. Prior to the time of maximum liquid-phase penetration, the maximum downstream extent of the vapor is the same as that of the liquid. After the liquid reaches its maximum penetration, the vapor-phase fuel continues to penetrate across the chamber, as shown in Fig. 11. The width of the vapor region increases in approximately a linear fashion downstream from the point where it is first observed. As a result, it is about twice as wide as the liquid by an axial location just upstream of the maximum liquid-fuel penetration (*i.e.* the location where the liquid fuel typically has its greatest breadth, just before it begins to narrow, about 2 mm upstream from the tip of the liquid region, see Fig. 10).

The data of Naber and Siebers [27] and Siebers [50] also indicate a similar distribution of vapor-phase fuel along the sides of the liquid-fuel region. Using combined schlieren and extinction photography which is sensitive to both vapor- and liquid-phase fuel, they [27] showed that the outline of a vaporizing diesel fuel jet has nearly a constant cone angle (for a given set of operating conditions) beginning at the injector and spreading outward downstream. An example of one of these images from Ref. [27] is reproduced in Fig. 12. Subsequent to these schlieren/extinction measurements, Mie-scatter images of the liquid-phase fuel were obtained, that appear very similar to those in Fig. 10 [50]. A comparison of these two image types shows that the spread of the liquid fuel distribution in the Mie images is much less than that of the outer cone of the jet seen in the corresponding schlieren images. This indicates a vapor region along the sides of the liquid-fuel of the same general shape as that found by Hodges et al. [18].

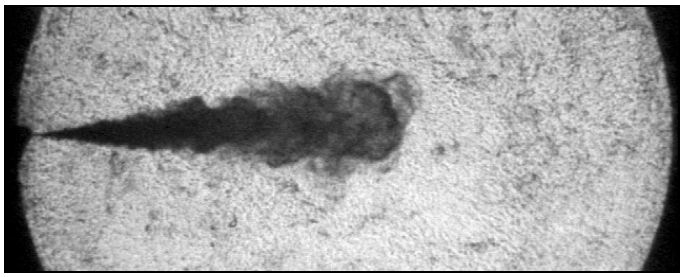

Figure 12. Reproduced from Naber and Siebers [27], with permission. A schlieren/extinction image of a vaporizing diesel fuel jet 1.2 ms ASI. The ambient density is 28.6 kg/m^3, and the temperature is 1000 K. The window diameter is 114 mm.

A comparison of the images in Figs. 10 and 11 also indicates a vapor fuel region along the outside of the liquid region similar to that described in the previous two paragraphs. A scale measurement shows that the width of the vapor fuel at the left edge of the images in Fig. 11 (27 mm from the injector) ranges from 4.5 to 8 mm. This is substantially greater than the 2.5 to 3 mm width of the liquid just 6 mm upstream (21 mm from the injector) where the liquid-fuel distribution reaches its maximum width. The schlieren diesel-jet cone-angle data of Naber and Siebers [27] for a similar operating condition (Fig. 13b of Ref. [27]) indicate a jet width of 6.5 mm at a point 27 mm from the injector. Considering the variation between the images in Fig. 10, this agreement is excellent. At 21 mm from the injector, the cone-angle data of Naber and Siebers indicates a jet width of 5 mm. This is about twice the liquid width at this point in very good agreement with the liquid-vapor width ratio found by Hodges et al. [18].

Putting all these data together, for the base operating condition we would expect to see a vapor-fuel region begin to form along the sides of the liquid fuel about 7 to 8 mm from the injector. This vapor-fuel region would then grow conically downstream so that at 21 mm from the injector it is about twice as wide as the liquid fuel, and at 27 mm it matches the vapor-fuel widths in Fig. 11.

AUTOIGNITION

Although the autoignition point is commonly defined as the crank angle when the apparent heat release rate reverses direction or first goes positive, natural flame emission has been noted prior to this time [34, 51, 52]. As discussed in Ref. [34], this early, relatively weak flame emission is due to chemiluminescence, which is created by energetic chemical reactions and is thought to closely mark the occurrence of combustion heat release both temporally and spatially [53-55]. As such, chemiluminescence imaging is a useful tool for examining autoignition in diesel combustion, with the limitation that the images are integrated along the line of sight.

Chemiluminescence Imaging - For the base operating condition and the reference fuel, chemiluminescence images were obtained as early as 3.5° ASI, and the first chemiluminescence may occur even earlier, as discussed in Ref. [34]. This is well before the minimum point on the heat release rate curve. These images show a weak emission across the downstream portion of all eight fuel jets in all engine cycles. At this crank angle (3.5° ASI), the vapor fuel has not penetrated much beyond the liquid, and most of the chemiluminescence occurs in the vapor at the sides of the jet in the region from about 13 mm from the injector to the tip of the vapor (about 25 mm from the injector). From 3.5° to 5.0° ASI, the entire downstream portion of all eight jets continues to emit chemiluminescence, the emission grows much brighter, and it shifts downstream from the injector as the fuel jet continues to penetrate across the chamber. By 4.5° ASI, the chemiluminescent region extends from about 16 mm to the tip of the vapor at about 34 mm from the injector. Since the maximum liquid penetration is 23 mm and the chemiluminescence is much brighter downstream of this point, most of the chemiluminescence is coming from the pure vapor-fuel region at the front of the jet by this crank angle.

The left hand column of Fig. 13. shows a temporal sequence of natural flame emission images from 4.5° to 6.0° ASI, reproduced from Ref. [34]. These images were obtained through the cylinder-head window with the same field of view as the vapor-fuel images in Fig. 11. The number in the upper right of each image gives the relative intensifier gain in arbitrary units [34]. The first image shows chemiluminescence* arising from the entire downstream portion of the fuel jet. By

* As discussed in Ref. [34], a spectral filter was used to verify that this emission was due to chemiluminescence rather than early luminous soot emission. In addition, its intensity is much lower than that of the soot luminosity which begins later.

5.0° ASI, the chemiluminescence is about twice as bright (note that the intensifier gain has been turned down) and still nearly uniform over the leading portion of the jet. Then, at 5.5° ASI a much brighter region appears over about half of the viewed portion of the jet, while the intensity over the remainder of the jet is about the same as in the previous image. The size, shape, and location of the brighter region varied randomly from cycle to cycle. Since the earlier images show that chemiluminescence intensity is increasing only slowly, this sudden large increase in image intensity most likely arises from early soot luminosity [34].

By 6.0° ASI, the emission is much more intense throughout the leading portion of the jet. The brightest areas are 60 times brighter than the brightest parts of the 5.5° ASI image and about 1200 times brighter than the chemiluminescence at 5.0° and 5.5° ASI. The intensity of this emission and the presence of soot detected by planar LII (discussed below) indicate that soot luminosity dominates the emission by 6.0° ASI. Beyond 6.0° ASI, the jet continues to grow, and the intensity of the luminosity increases, eventually becoming more than 60 times brighter than the last image in Fig. 13.

It should be noted that for all engine cycles, the chemiluminescence was found to arise gradually over the entire downstream region of all the fuel jets. It was never isolated to certain regions that might suggest the progression of the reaction zone along the jet either axially or from side to side. This fact, combined with the length and time scales of these chemiluminescence images, indicates that ignition must be occurring at multiple points nearly simultaneously [34]. However, because these images are integrated along the line of sight through the jet, they do not show whether the reaction is confined to the peripheral regions (surface) of the jet or is volumetric.

PAH Imaging - To help determine whether the early combustion is volumetric or confined to the surface, planar laser-induced fluorescence (PLIF) images of the PAH emission were obtained, and they are presented in the right hand column of Fig. 13. The field of view is approximately the same as for the natural emission images. A horizontal laser sheet was used, and the image plane is 9 mm below the cylinder head.

To avoid any fluorescence signal from the fuel, a 387 nm laser was used. Although the reference fuel constituents do not fluoresce with excitation in the 250 to 400 nm range, the best commercially available grade of these compounds showed a significant fluorescence at wavelengths shorter than about 370 nm due to trace impurities. The 387 nm excitation eliminated signal from unreacted fuel, but made the measurement sensitive only to larger PAHs that fluoresce with this relatively long-wavelength excitation [56]. In addition, 387 nm excitation could excite CH fluorescence [57], but analysis of the PLIF emission spectrum (using as series of narrow-band-pass filters) showed that this was not significant relative to the broadband PAH signal. The PAH images in Fig. 13 were obtain using a 410 nm long-wave-pass filter to eliminate elastic scattering and maximize the signal by integrating over most of the broad PAH emission band.

The first PLIF image in Fig. 13 shows no significant PAH signal at 4.5° ASI, despite the chemiluminescence occurring across this same region of the fuel jet. (Higher camera gains were tried, but they did not improve signal to noise.) Beginning at 5.0° ASI a relatively strong PAH signal appears that is nearly uniform over the cross section of the leading portion of the fuel jet. This timing coincides exactly with the breakdown of fuel across the jet cross section shown in Fig. 11. At 5.5° ASI, the PAH distribution is similar although it extends further as the jet continues to penetrate. Then at 6.0° ASI, some very bright regions appear. In the image shown, they extend inward from around the leading edge and also occur in the upstream region. The shape and location of these bright regions varied randomly from cycle to cycle, but they always filled a significant portion of the jet cross section. This sudden increase in signal intensity, combined with the soot luminosity in the corresponding natural flame emission image, indicate that these bright regions are almost certainly due to LII from the early soot. In addition, standard LII images presented in the next subsection show soot beginning at this crank angle.

As discussed above, the chemiluminescence images do not show whether the reaction is volumetric or confined to the

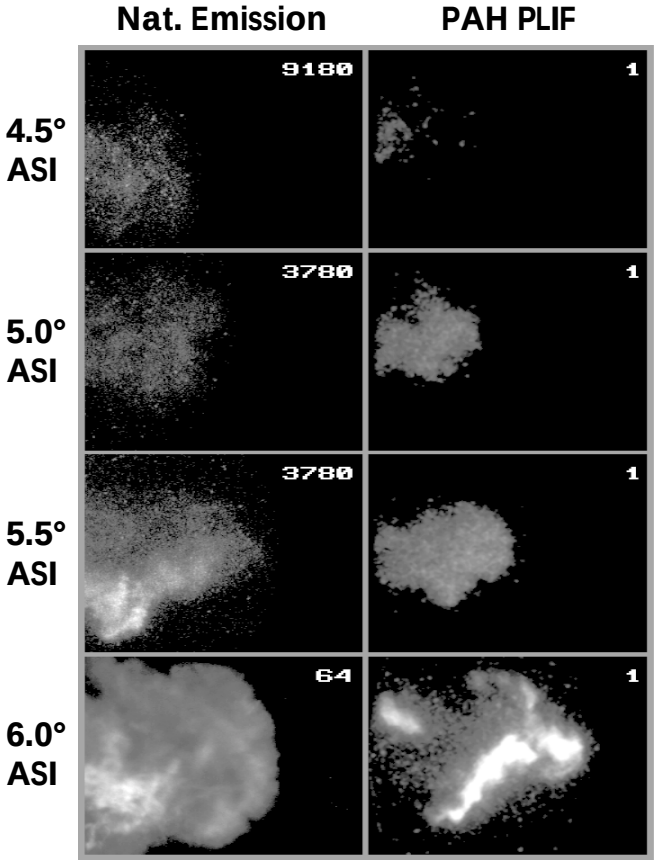

Figure 13. Temporal sequences of semi-quantitative natural flame emission images (left) and PAH fluorescence in the 9 mm plane (right), using the reference fuel. The left edge of the images is 27 mm downstream from the injector, and the field of view is approximately 18 mm by 13 mm. The crank angle degree ASI is given at the side of the images, and at the upper right of each image is the relative intensifier gain in arbitrary units.

jet periphery. Although the spatially resolved vapor-fuel and PAH images do not exhibit activity during the early chemiluminescent period, starting between 4.5° and 5.0° ASI, they show the vapor fuel breaking down (Fig. 11) and PAHs forming (Fig. 13) almost uniformly throughout the cross section of the leading portion of the jet. This is followed, 140 μs later, by soot formation throughout the cross section as will be shown in the next subsection. In addition, the timing of the major fuel breakdown coincides with the start of the rapid rise in the heat release rate at the start of the premixed burn. These combined data indicate that the majority of the premixed burn occurs volumetrically throughout the cross section of the leading portion of the jet.

EARLY SOOT FORMATION

Figure 14 shows simultaneous LII (left) and elastic-scatter (right) images of the early soot formation, adapted from Ref. [34]. This temporal sequence begins at 6.0° ASI when the first soot can be detected with planar imaging and continues until near the end of the premixed burn spike. Like the images in Figs. 11 and 13, the laser sheet was horizontal in the plane 9 mm below the cylinder head, and the left edge of the image is 27 mm (along the fuel-jet axis) downstream of the injector. The field of view has been increased to 26 by 18 mm to accommodate the fuel jet at the later crank angles. The first two image pairs (6.0° and 6.5° ASI) were taken with the reference fuel, while the rest of the sequence was obtained with the low-sooting fuel #1. This change in fuels was necessary because significant optical attenuation occurs with the reference fuel beginning at 7.0° ASI. A complete comparison, given in Ref. [34], shows that the ignition and early soot formation of these two fuels is virtually identical up to the point when soot obscures the reference-fuel images.

As discussed in the Background Section (subsection entitled Early Laser-Sheet Imaging Studies) the LII image intensity provides a measure of the relative soot concentration (volume fraction), while the elastic scatter image intensity is biased to regions of larger soot particles. By comparing the elastic scatter images (intensity proportional to d^6) with the LII images (intensity proportional to d^3), the relative soot-particle size distribution may be deduced [33, 34]. An edge filter was used to split the optical signal into two cameras. A 450 nm short-wave-pass filter was used on the LII camera and a 532 nm narrow-band-pass filter was used on the elastic-scatter camera [34].

The first soot was detected at 6.0° ASI with LII only. It occurred across wide portions of the cross section of the leading part of the jet, at locations that varied randomly from cycle to cycle. The LII image in Fig. 14 is typical of those at 6.0° ASI, in that the soot is in the center of the jet as well as the edge, but in some cycles there is more soot near the leading edge and less upstream than in the image presented. In the simultaneous elastic-scatter image, the area of strongest signal does not coincide with the sooting regions evident in the LII image. This indicates that the elastic-scatter signal arises from fuel vapor and that the first soot particles must be very small since they give an elastic-scatter signal that is significantly weaker than that of the vapor-fuel/air mixture [34]. These small soot particles which appear throughout the cross section of the jet are thought to be formed by the fuel-rich premixed burn, as discussed in the previous subsection and in Ref. [34].

By 6.5° ASI (70 μs later), the LII image shows soot occurring throughout the cross section of the leading portion of the jet with the highest soot concentrations being more than 2.5 times greater than at 6.0° ASI. The corresponding elastic scatter image continues to show a weak signal from the central region of the jet, but now it also contains a high-signal region around the periphery of the jet. This elastic-scatter signal from the periphery is much stronger than that of the vapor fuel prior to fuel breakdown, and the outline of this high-intensity region exactly matches the outline of the soot in the LII image. Therefore, it must indicate the presence of soot particles. Moreover, these soot particles around the periphery must be much larger than those in the center of the jet since the elastic-scatter signal intensity varies greatly while the LII image shows almost the same soot concentration in both regions. Since there is no evidence of these larger soot particles in the previous image, they must become large much more rapidly than those in the center of the jet. This suggests that a different mechanism is responsible for their formation or growth rate. As will be shown later, this timing coincides with the formation of a diffusion flame around the jet periphery between 6.0° and 6.5° ASI, just before the mid-point of the premixed burn spike (see Fig. 8a).

Starting with the 7.0° ASI images, the low-sooting fuel #1 was used because optical attenuation became significant with the reference fuel. Small soot particles continue to appear throughout the majority of the jet cross section, and the soot concentrations at 7.0° ASI have increased significantly from those at 6.5° ASI [34] although this is masked in Fig. 14 by the switch to the low-sooting fuel. The corresponding elastic scatter image shows that the region of larger soot particles at the periphery has become somewhat thicker. This is presumably the result of turbulent eddies transporting the larger soot from near the surface of the jet inward since OH images (presented later) show that the diffusion flame remains confined to the jet periphery.

From 7.0° ASI through the end of the sequence at 8.5° ASI, the images in Fig. 14 show a progressive development of the soot distribution. Soot occurs throughout the majority of the cross section of the leading portion of the jet, and its concentration continues to increase as indicated by the intensifier gain numbers. For the later crank angles (7.5°-8.5° ASI), soot concentrations are generally higher toward the front of the jet and lower upstream; however, at any axial location, the soot concentration is approximately the same in the center and at the periphery of the jet. The elastic-scatter images show that large particles remain generally confined to the peripheral regions during these early stages of diesel combustion. As the fluid mechanics continue to act on the combusting jet, the large-particle region at the periphery becomes thicker, particularly at the front of the jet, but there are few large particles in the central region even at 8.5° ASI (near the end of the premixed-burn spike).

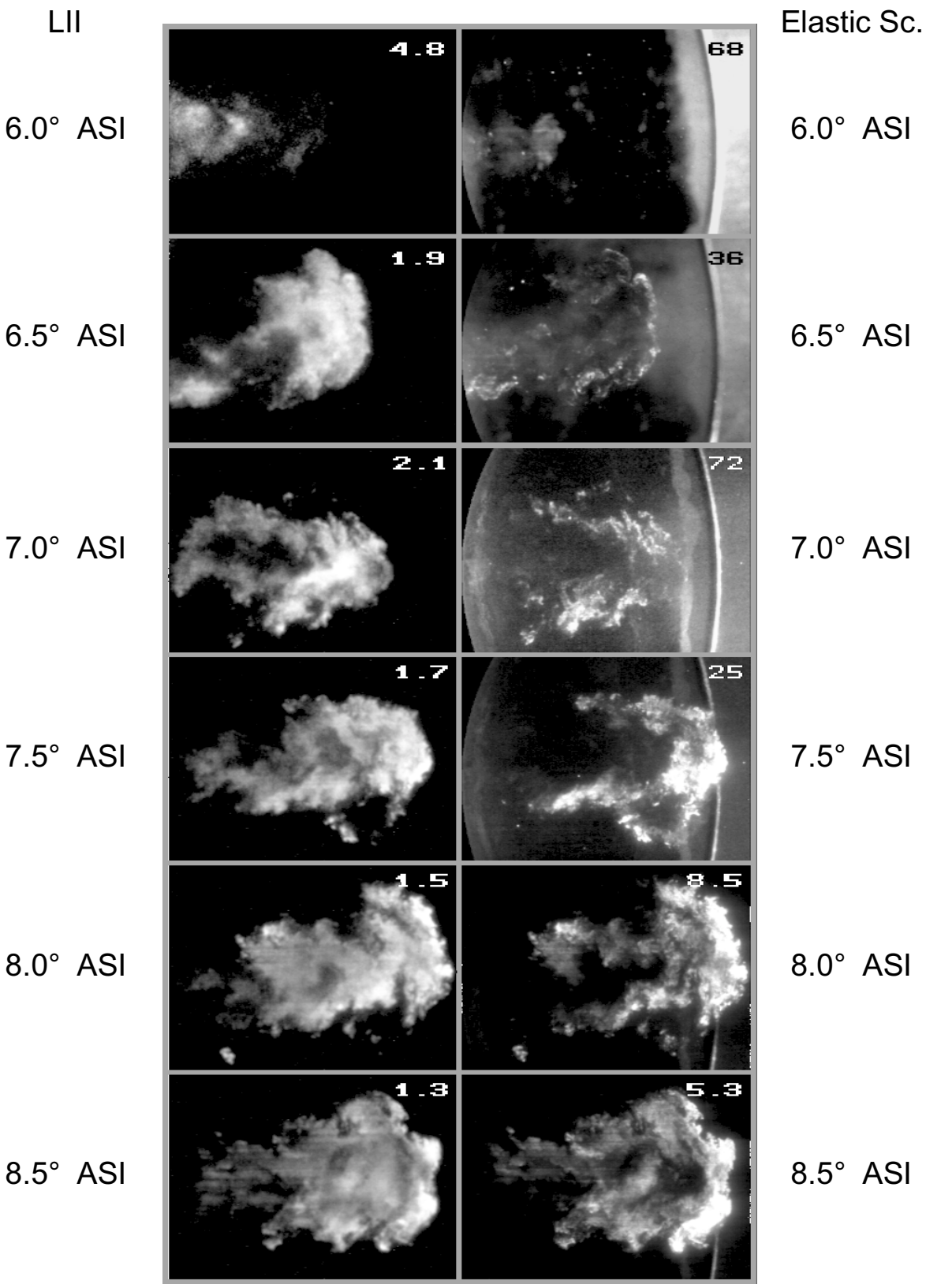

Figure 14. Adapted from Dec and Espey [34]. Temporal sequence of simultaneous LII and elastic scatter images in the plane 9 mm below the cylinder head. For each image pair, the LII image is at the left and corresponding elastic scatter image is at the right. The first two image pairs (6.0° and 6.5° ASI) were obtained using the reference fuel and the remainder of the set was obtained using the low-sooting fuel #1. The left edge of the image is 27 mm downstream from the injector nozzle, and the field of view is 26 mm by 18 mm. The crank angle degree ASI is given at the side of each image, and the upper right of each image is the relative intensifier gain in arbitrary units.

LATER SOOT DISTRIBUTIONS

Figure 15 shows temporal sequences of natural soot luminosity, LII, and elastic-scatter images through the mixing-controlled burn for the high fuel-load condition (longer injection duration).* The LII and elastic-scatter images were taken with the laser sheet on the fuel jet axis, and the magnification was adjusted so that the entire view through the cylinder-head window was imaged, see Fig. 9. The black line around each image shows the limits of this field of view which is 43.5 mm wide and 48 mm high in maximum dimensions. As discussed in the subsection on Operating Conditions and Fuels, the low-sooting fuel #2 was used to minimize optical attenuation. The intake conditions were adjusted to provide a lower TDC temperature so that the ignition delay and heat release rate were similar to those used previously despite the higher cetane number of this fuel (see Table 4). This lower temperature may cause a slightly longer maximum liquid-fuel penetration; however, the lower boiling point of the main constituent of the low-sooting fuel #2 will tend to compensate for this. At the most, the maximum liquid length is only 2 or 3 mm longer than that of the reference fuel since it is never visible through the cylinder-head window. Unlike the images in Figs. 6 and 14, the LII and elastic-scatter images in Fig. 15 are not simultaneous but have been selected from image sets from different engine cycles. The signal intensities have been mapped to the same blue-red-yellow false color scale used in Fig. 6. The sequence is broken into two parts, Fig. 15a and 15b. The first image in Fig. 15a overlaps the earlier soot sequence in Fig. 14, and the last image in Fig. 15a (17° ASI) is repeated as the first image in Fig. 15b to facilitate following the two-part sequence.

The natural soot luminosity images in the top row give a general picture of the luminous (sooting) combustion. Because the plume has a low optical density when the low-sooting fuel is used, these images provide a picture of the natural soot luminosity integrated along the line of sight through the plume. Note that the soot luminosity images show the extent of the sooting region to be approximately the same as in the corresponding LII images. All the luminosity images, except the one at 7.0° ASI, were taken with the same intensifier gain and camera aperture so image intensities at the different crank angles can be compared. The 7.0° ASI image required a wider camera aperture because the luminosity was much weaker, so the intensity cannot be compared with the other images.

As discussed previously, the LII image intensity provides a measure of the relative soot concentration, while the elastic-scatter image intensity is biased to regions of larger soot particles. For both the LII and elastic-scatter images, the same intensifier gain and camera aperture were used for the entire sequences so intensities can be compared. The on-axis laser sheet orientation results in the laser light impinging on both the liquid fuel and cylinder head. This contributes a background signal to the elastic-scatter soot images. As a result, all the elastic-scatter images, except the one at 9.0° ASI, have been partially corrected by subtracting a background image obtained with no fuel injection. No elastic-scatter image is presented at 7.0° ASI because it could not be distinguished from the comparatively strong background with this laser-sheet orientation (refer to Fig. 14 for an elastic-scatter image).

First Part of the Mixing-Controlled Burn - The first LII image (7.0° ASI) in Fig. 15a was obtained during the latter part of the premixed burn (see Fig. 8b), and it is similar to the one in Fig. 14. Soot is present throughout the cross section of the luminous region of the fuel jet, with a slightly higher concentration at the leading edge. Then by the start of the mixing-controlled burn at 9.0° ASI, a pattern develops of a higher soot concentration in the head-vortex region and a lower concentration upstream. This soot concentration pattern persists through the remainder of the sequence in Fig. 15a as the overall soot concentration increases and the combusting fuel jet penetrates to the cylinder wall.

The LII images in Fig. 15a show the upstream extent of the soot distribution to be approximately at the left edge of the cylinder-head window (27 mm from the injector). This is particularly evident in the 7.0° to 11.0° ASI images but is less obvious in the later images which appear to have some attenuation effects, particularly in this upstream region. This upstream limit to the soot distribution is also supported by the corresponding soot luminosity images. In addition, the 9.0° and 11.0° ASI LII images show that even after the premixed burn is complete, soot still appears across the entire jet cross-section (at the center as well as along the edges) at this same upstream location. To verify these findings, additional LII images were taken through the piston-crown window with the laser sheet on the fuel-jet axis. These images showed that the upstream extent of the soot remained within a few millimeters of this 27 mm location throughout the first part of the mixing controlled burn (from 9.0° ASI to the end of injection). They also showed that the soot appeared across the entire jet cross-section at this location, similar to the 9.0° and 11.0° ASI images in Fig. 15a.

The first elastic-scatter image presented is at 9.0° ASI, and it shows a similar distribution to the brightest regions of the 8.5° ASI elastic-scatter image in Fig. 14. However, the background scatter is greater in the 9.0° ASI image due to the laser sheet orientation. In the 9.0° ASI image, the signal is stronger, indicating larger particles, around the periphery of the leading edge with a weaker signal upstream that is barely distinguishable from the background scatter. By the time of the next image (11° ASI), the elastic-scatter signal has become much stronger throughout most of the head vortex. This increase in signal must be due to an increase in soot-particle size since the corresponding LII image shows that the soot concentration has increased only slightly from 9.0° ASI.

This same general size-distribution pattern continues through the rest of the sequence in Fig. 15a. Note that for the 11° to 17° ASI images, the weaker elastic-scatter signal upstream (which was only slightly stronger than the background, similar to the 9° ASI image) was almost completely

* These images have not previously been published, although they were presented at a conference and written up as a limited-distribution report [35].

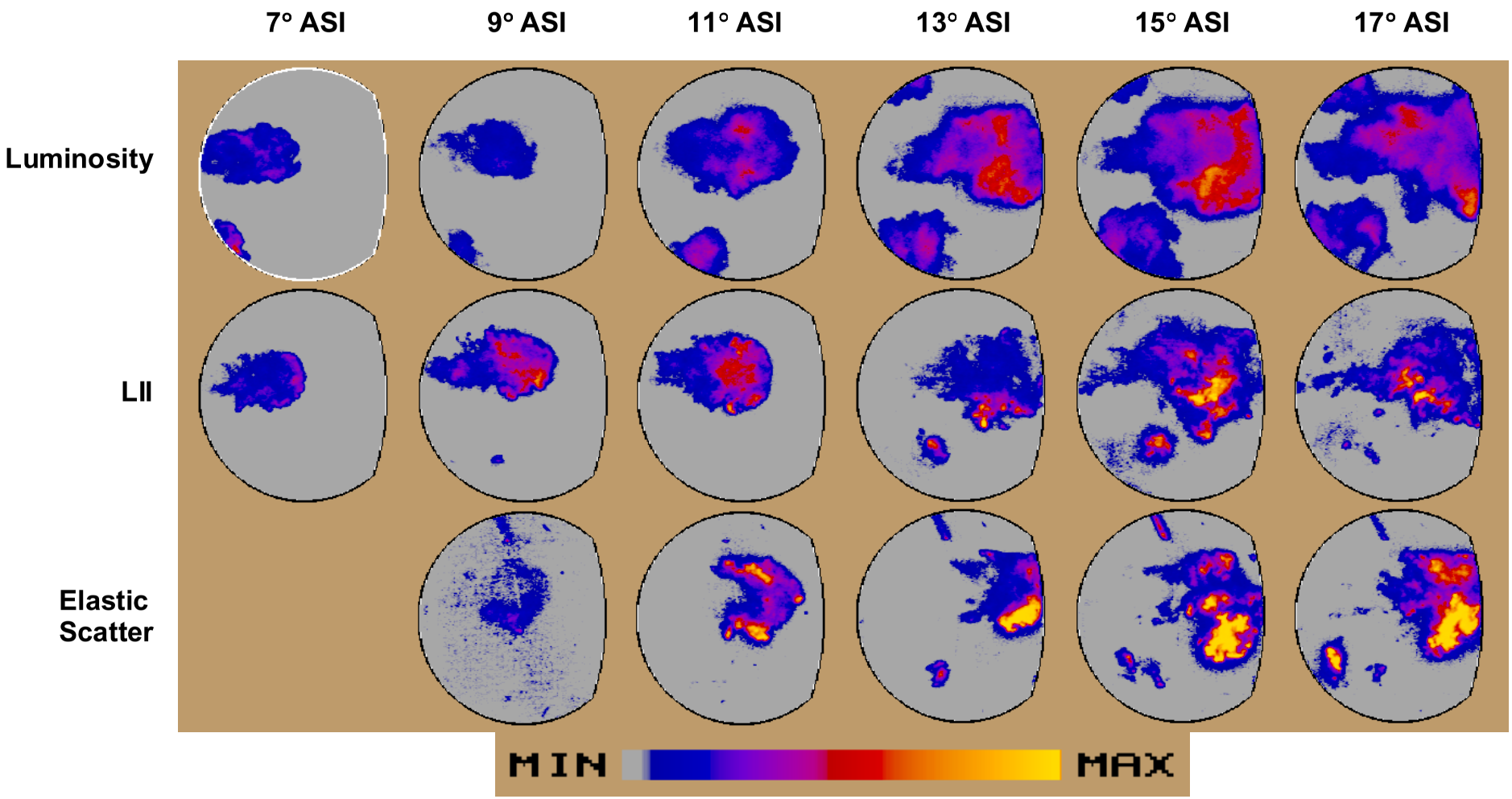

Figure 15a. Part 1 (7° to 17° ASI) of a temporal sequence of natural soot luminosity, laser-induced incandescence (LII), and elastic-scatter images for the high-load operating condition. The crank angle degree ASI is given at the top of each set. The fuel is the low-sooting #2, and the average equivalence ratio is 0.43. The white border around the 7° ASI image indicates that it was taken at a higher camera gain than the rest of the set.

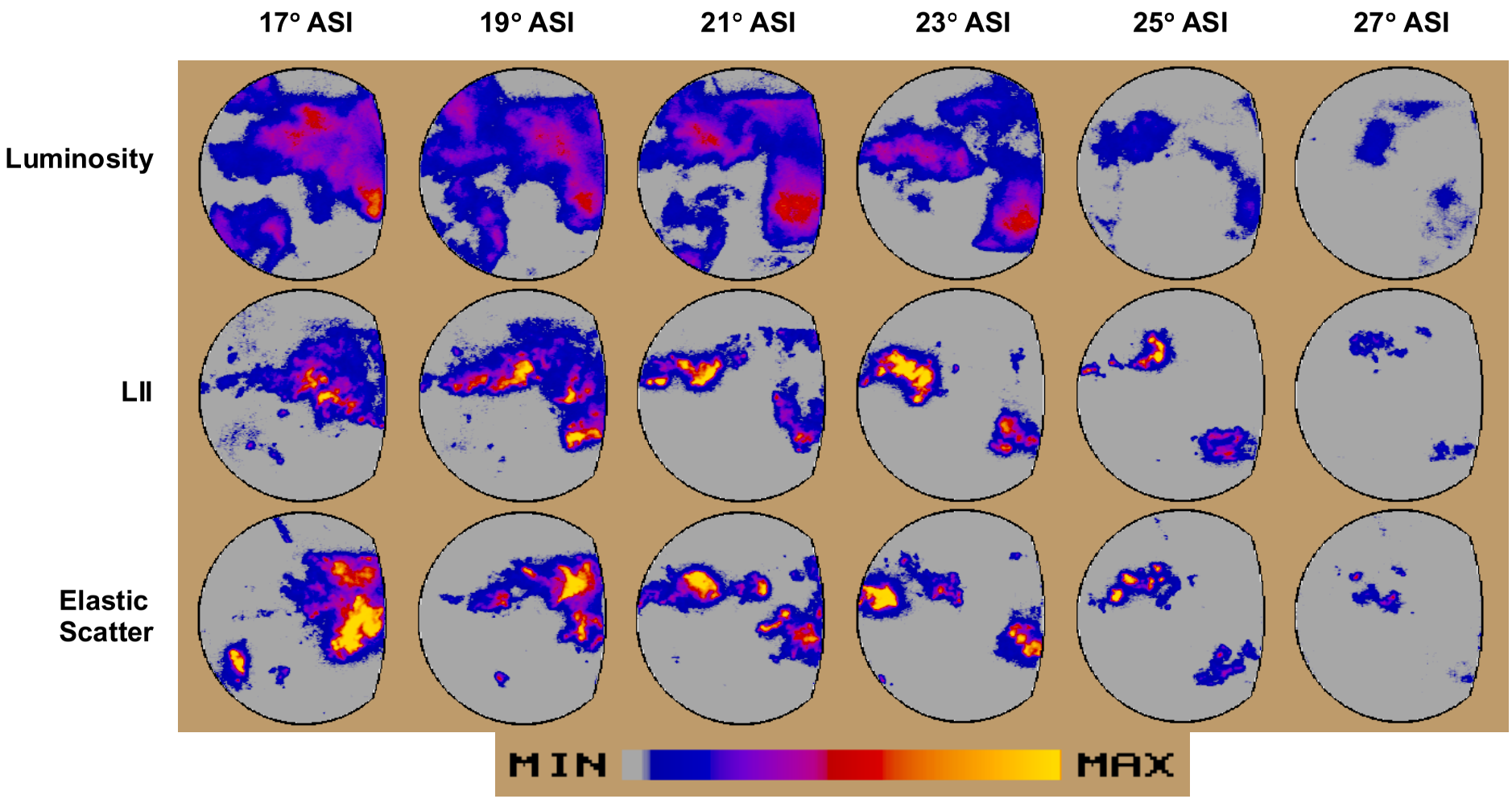

Figure 15b. Part 2 (17° to 27° ASI) of a temporal sequence of natural soot luminosity, laser-induced incandescence (LII), and elastic-scatter images for the high-load operating condition. The crank angle degree ASI is given at the top of each set. The fuel is the low-sooting #2, and the average equivalence ratio is 0.43.

lost when the background was subtracted.* Accordingly, these images show that as the mixing-controlled burn progresses, the soot particles in the head vortex become much larger, while the soot particle-sizes upstream of the head vortex remain similar to those at earlier crank angles.

The combination of images from 11° to 17° ASI shows that throughout the first part of the mixing-controlled burn: 1) soot is present throughout the cross section of the combusting fuel jet beginning near the left edge of the field of view (about 27 mm from the injector), 2) in the upstream part of this sooting region, the soot concentration is lower and the soot particles are smaller, and 3) downstream, in the head-vortex region, the soot concentration is higher and the soot particles are larger. This distribution suggests a history to the soot formation with the soot initially forming as small particles at about 27 mm, and additional formation and particle growth continuing as the soot moves down the jet into the head vortex. This soot concentration and size-distribution pattern persists through the remainder of the fuel-injection period, until about midway through the mixing-controlled burn for this operating condition.

Latter Part of the Mixing-Controlled Burn - Immediately following the end of injection, the images in Fig. 15b show a distinct change in the soot distribution pattern. For this operating condition, injection ends at about 18.5° ASI (9° ATDC) as shown in Fig. 8b.** At 19° ASI, the LII image shows a higher soot concentration developing in the upstream portion of the jet. Similarly, the elastic-scatter image intensity is also higher in the upstream region, indicating that there are now larger particles in the upstream region. By 21° ASI, the new soot-distribution pattern is well developed. There is a high soot concentration and larger soot particles in the upstream region of the jet as well as in the remains of the head vortex. This pattern persists with the soot concentration slowly decreasing for the remainder of the image sequence. By the time of the final image in Fig. 15b the heat release is nearly complete, as shown in Fig. 8b.

It is thought that this change in the soot distribution with the end of injection occurs as a result of the injector needle throttling the flow through the injector holes as it closes. This causes the last fuel to be injected at a lower velocity than the previous fuel, so it cannot catch up with the leading edge of the jet, and it is probably not as well atomized as the fuel injected prior to needle closure. As a result, this last fuel does not mix well with the in-cylinder air but remains along the fuel-jet axis. This leads to a high degree of soot formation and soot particle-size growth. In support of this hypothesis, it should be noted that the changes in the soot distribution with the end of injection seen in Fig. 15b, were not noticed by the author in a previous study in a similar research engine fitted with a Cummins PT open-nozzle injector which was designed so that the last bit of fuel is forced out under high pressure.

Finally, Fig. 15b shows that the pockets of high soot concentration and large soot particles along the jet axis persist well into the expansion stroke, and are still present near the end of the heat release. Although we have not made measurements of the tail pipe emissions from this engine, it is possible that these pockets of soot which are formed near the end of injection do not oxidize well and contribute preferentially to particulate emissions.

DIFFUSION FLAME DEVELOPMENT

Figure 16 presents a temporal sequence of OH-radical PLIF images showing the diffusion flame development, reproduced from Ref. [14]. Similar to the liquid-fuel images in Fig. 10, these images were obtained through the piston-crown window with the laser sheet oriented along the axis of the jet in the 3-o'clock position. The filter set used allowed some of the strong elastic scatter from the liquid fuel to be visible as well as the OH signal [14]. In the first several images, the location of the injector tip is evident at the left edge along with a strong liquid-phase fuel signal from 5 of the 8 fuel jets. The gray curve at the right marks the edge of the combustion bowl (see Fig. 9), and the horizontal distance from the injector to the edge of the bowl is 49 mm. As discussed previously with respect to Fig. 10, all eight fuel jets are very symmetric [13] although the liquid fuel distribution appears unequal in Fig. 16 due to nonuniform illumination and laser-sheet attenuation (discussed below). The low-sooting fuel #1 was used for these images.

The sequence begins at 5.0° ASI. This first image shows a strong elastic scatter signal from the liquid-phase fuel, but there is no detectable OH. At this crank angle the premixed vapor-fuel/air region of the jet extends well out beyond the liquid phase and the premixed burn is well underway, as evident in Figs. 11 and 13. The dashed line in first two images in Fig. 16 indicates the approximate extent of the reacting vapor-fuel/air mixture. There is no OH signal from this premixed burn because it is so fuel rich (equivalence ratio of 2 to 4, see Fig. 11) that OH is virtually non-existent [14]. Thus, for typical diesel combustion, high OH concentrations arise only from the diffusion flame where combustion is near stoichiometric. Moreover, these high OH concentrations are confined to a very narrow region around the diffusion flame because of the high rate at which flame-front OH-super-equilibrium concentrations are reduced to equilibrium levels at diesel pressures, and because OH equilibrium concentrations drop rapidly outside of a diffusion flame. A full discussion of this may be found in Ref. [14]. Accordingly, the OH PLIF signal closely marks the diffusion flame zones.

At 5.5° ASI, the first indication of OH is seen at the sides of the premixed-combustion area. In the image presented, the region labeled "a", is on the periphery of the fuel jet in the 3 o'clock position and the brighter region labeled "b" is in a similar location on the adjacent fuel jet. By 6.0°

* There is still some evidence of larger soot particles (larger than the particles in the center of the jet, but smaller than those in the head vortex) along the sides of the jet in the upstream region. Both the 13° and 15° ASI images (and to a lesser degree the 17° ASI image) show an elastic-scatter signal extending upstream from the head vortex for several millimeters along either side of the jet before the signal becomes too weak see.

** Note that start of injection is 9.5° BTDC for this high-load data (see Table 4 and the subsection on Data Acquisition and Optical Setup).

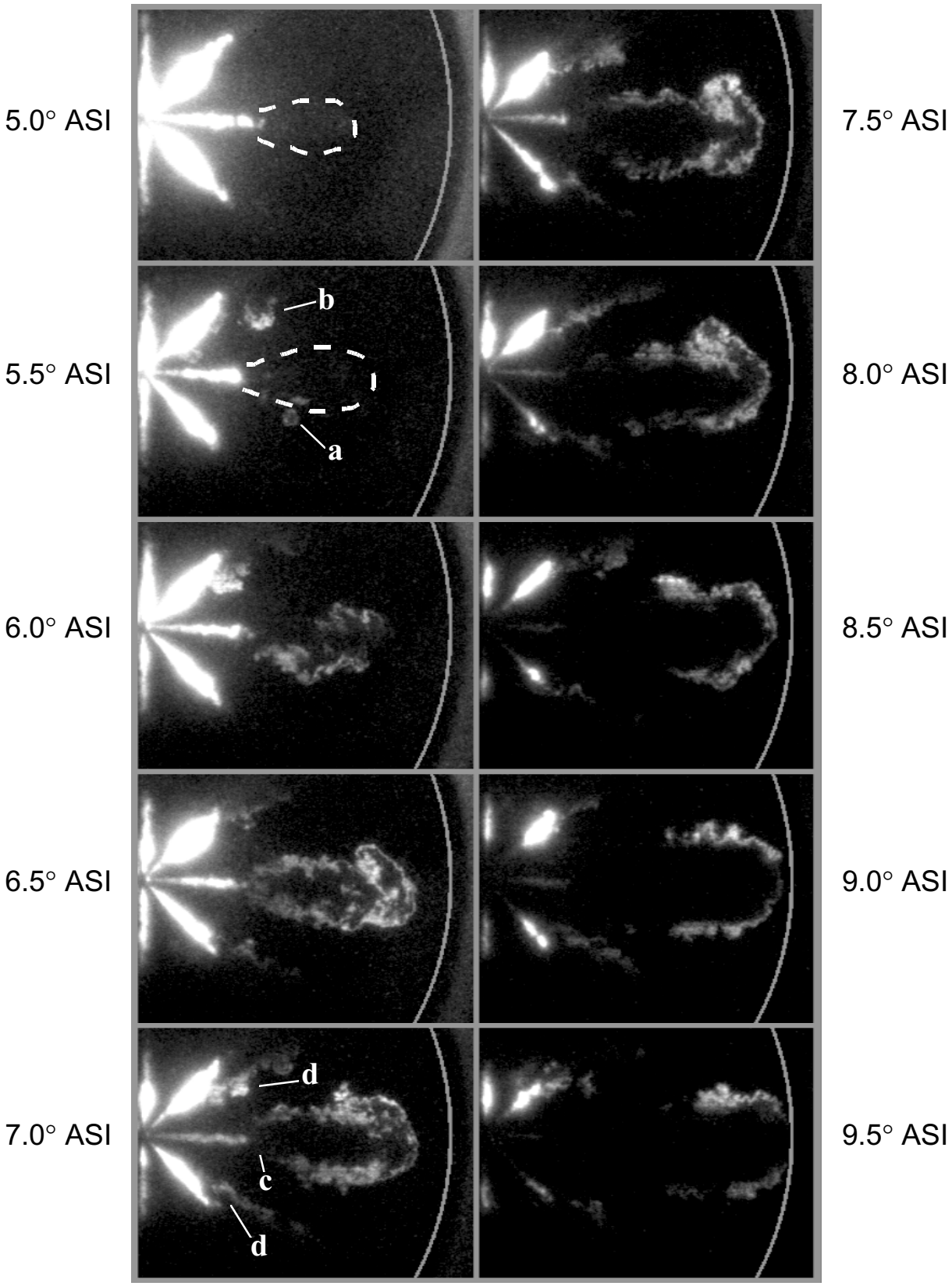

Figure 16. Reproduced from Dec and Coy [14]. Temporal sequence of OH PLIF images obtained through the piston-crown window with the laser sheet on the fuel-jet axis. The crank angle degree after the start of injection (ASI) is given at the side of each image. The rectangular field of view is 54 mm by 41 mm, and the gray curve shown in the right of each image indicates the edge of the combustion bowl (also the limit of the field of view through this window, see Figs. 7 and 9). The labels “a”, “b”, “c”, and “d” are explained in the text.

ASI, the PLIF image shows OH extending around a large fraction of the periphery of the leading portion of the jet. Then, at 6.5° ASI, the leading portion of the reacting fuel jet is completely surrounded by a thin layer of OH that extends back toward the injector to a point just upstream of the tip of the liquid fuel. Through the rest of the sequence, OH is present around the periphery of the downstream portion of the combusting jet. As discussed above, this OH signal indicates that a diffusion flame has formed around the jet periphery. Eventually, the fuel-rich premixed burn progresses to the point where temperatures and radical concentrations are sufficiently high for a diffusion flame to develop at the interface between the partially reacted premixed region (which contains significant excess fuel) and the surrounding air.

It should be noted that the diffusion flame has been established around the jet periphery at 6.5° ASI, which is the same crank angle that Fig. 14 shows large soot particles suddenly appearing at the jet periphery. This coincidence in both timing and spatial location is strong evidence that the diffusion flame causes the formation of the large soot particles at the jet periphery.

Attenuation effects on the OH signal are evident beginning with the 7.0° ASI image. In this image, OH exists around the periphery of the 3 o'clock fuel jet in a pattern similar to the 6.5° ASI image except that the signal is weak or nonexistent in the upstream regions, labeled "c". However, OH must be present in this region since a strong signal is clearly visible along the sides of the two adjacent fuel jets in this same upstream region (areas labeled "d"). As the laser traverses the length of the 3 o'clock fuel jet, it is attenuated by absorption and/or scattering. The OH signal is much brighter in the upstream regions of the two adjacent jets since the laser sheet has not yet been attenuated. There can also be attenuation of the signal between the plane of the laser sheet and the camera, although for most cases this is of lesser importance because the path length is much shorter than the laser path along the jet axis.

Although attenuation becomes progressively worse through the rest of the sequence, the general nature of the diffusion flame can still be seen toward the leading edge and in the upstream region of the adjacent jets.[*] It remains confined to a relatively thin region around the extreme periphery of the fuel jet, and the upstream end of the diffusion flame remains back along the sides of the tip of the liquid-phase fuel.[**] Since there is no indication of the diffusion-flame location changing up to when the sequence ends at the start of the mixing controlled burn, these OH data suggest that the diffusion flame remains at the jet periphery during the rest of the injection event. These findings are supported by the work of Kosaka et al. [23] who showed similar OH distributions up through the end of injection for diesel-like combustion of a low-sooting fuel in a rapid compression machine.

[*] Images at crank angles later than 9.5° ASI could not be obtained because soot almost completely obscured the OH signal.

[**] A complete discussion of the interpretation of these OH images including the thin sheet-like nature of the diffusion flame, the effects of turbulence on the OH distribution, and the effects of attenuation may be found in Ref. [14].

A CONCEPTUAL MODEL OF DI DIESEL COMBUSTION

This section presents a series of schematics that combine the information from the individual imaging measurements in the previous section into a comprehensive picture of DI diesel combustion. These composite schematics represent idealized cross-sectional slices through the mid-plane of the jet, and they show conceptually how DI diesel combustion occurs in the absence of wall interactions and swirl. Only a limited discussion is given with the presentation of the schematics. More complete discussions on each aspect of diesel combustion are available in the Data Presentation section and in the references cited.

TEMPORAL SEQUENCE OF SCHEMATICS

Figure 17 presents a temporal sequence of schematics showing the development of a diesel fuel jet from the start of injection, through the premixed burn, and into the first part of the mixing-controlled burn. These schematic images depict the base operating condition in our research diesel engine with a fuel loading that is sufficiently high for the injection duration to extend beyond the end of the sequence.[*] This is a typical operating condition for DI diesel combustion; however, for production engines the amount of turbocharger boost and intercooling and the injector characteristics can vary greatly, affecting both the temporal and spatial scaling (see for example Refs. [27, 29]). In Fig. 17, the crank angle degree after the start of injection (ASI) is given at the side of each image (1° = 139 μs), the scale is approximately 1.5:1, and the color scheme is shown in the legend at the bottom.

The schematics show an idealized single cycle with all components of the reacting jet being shown with an average position and shape. The jet is shown as penetrating to an average (typical) length, and the boundaries are drawn as smooth lines. In a real jet, there is always some cycle-to-cycle variation in the jet penetration and symmetry, and the boundaries are always ragged in appearance due to small-scale turbulence. Although the schematics depict a jet of approximately average size and shape, it is important to realize that they do <u>not</u> show a cycle-averaged picture of the jet which would tend to smear out gradients and the boundaries between components.

<u>Initial Jet Development (0.0° - 4.5° ASI)</u> - The first three images in Fig. 17 show the jet penetration out to the point where all the liquid is vaporized. The dark brown region labeled as liquid fuel shows the maximum extent of the liquid fuel droplets (the point at which the last droplets vaporize). At the injector, this region contains only liquid fuel, but downstream, air is entrained and fuel vaporizes so these gases are present along with the liquid-fuel droplets. Initially, liquid fuel (droplets, ligaments, and/or an intact liquid core) covers the cross section, as shown in the 1.0° ASI schematic. Then a vapor-fuel region begins to develop along the sides of the jet beyond the extent of the liquid droplets (2.0° ASI

[*] As discussed in the subsection on Operating Conditions and Fuels, for the injector used here, changing the amount of fuel injected changes only the injection duration and not the initial injection rate.

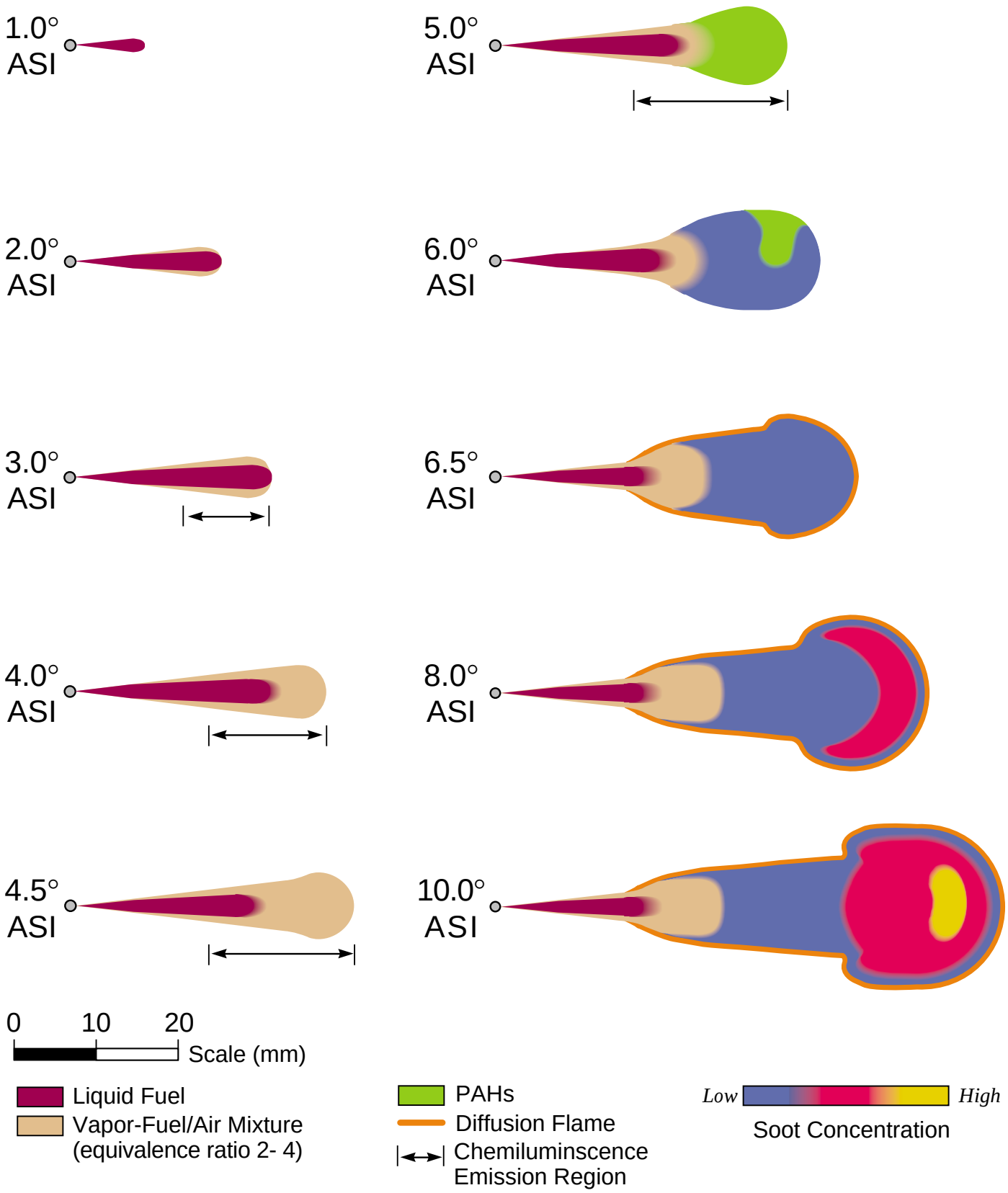

Figure 17. A temporal sequence of schematics showing how DI diesel combustion evolves from the start of injection up through the early part of the mixing-controlled burn. The temporal and spatial scales depict combustion for the base operating condition (a typical diesel engine condition, see Table 4) with an injection duration extending beyond the sequence shown. The crank angle degree ASI is given at the side of each schematic (1° = 139 μs).

schematic). This vapor region at the sides grows thicker as the jet continues to penetrate because the width of the liquid region increases more slowly than does the width of the overall jet (see Figs. 10 and 12). Then, at 3.0° ASI the liquid reaches its maximum penetration of about 23 mm. The entrainment of hot air into the jet has been sufficient to vaporize all the fuel by this point.

As seen in the subsequent images, the gas phase continues to penetrate across the chamber, and a head vortex eventually develops as is typical of penetrating gas-phase jets. By 4.5° ASI, the jet has penetrated to about 34 mm, and the leading portion contains a "relatively uniform" fuel/air mixture with equivalence ratios ranging from about 2 to 4. Although this range of equivalence ratios varies by a factor of two, compared to being near-stoichiometric or very fuel rich (too rich to support combustion even at these temperatures) it may be considered relatively uniform. As shown in Fig. 11, this fuel-rich but combustible mixture extends at least 6 or 7 mm upstream from the tip.

Autoignition (3.0° - 5.0° ASI) - The exact point of ignition is not well defined either temporally or spatially. Chemiluminescence occurs over the downstream portion of all the jets as early as 3.5° ASI. At this time the vapor has barely penetrated beyond the liquid, so this natural emission must be occurring in the vapor region along the sides of the jet. The chemiluminescent region of the jet is indicated in Fig. 17 by the arrows under the schematics. This is shown beginning with the 3.0° ASI schematic because there is no 3.5° ASI schematic and Ref. [34] indicated that chemiluminescence might actually begin earlier. It is not known whether this chemiluminescence occurs at the surface or more volumetrically through the vapor-fuel/air mixture. Initially (3.0° and 3.5° ASI) the vapor layer is not very thick, but by 4.5° ASI most of the chemiluminescence is coming from the large region of vapor-fuel/air mixture in the leading portion of the jet. In this region, it is very likely that the autoignition as marked by chemiluminescence occurs volumetrically since fuel breakdown and PAH formation occur volumetrically throughout this region between 4.5° to 5.0° ASI, followed by volumetric soot formation between 5.0° and 6.0° ASI.

First Part of Premixed Burn Spike (4.0° - 6.5° ASI) - The heat release rate curve (Fig. 8) starts to head up at 4.0° ASI and then increases very sharply after 4.5° ASI. By 4.5° ASI the leading portion of the jet is highly chemiluminescent as indicated in the schematics (see also Fig. 13), but there is little indication of significant fuel breakdown. Then within 70 μs (by 5.0° ASI), the fuel breaks down and large PAHs form almost uniformly across the entire cross section of the leading portion of the jet, where the equivalence ratio ranges from 2 to 4. This timing coincides with the rapid rise in the heat release rate indicating that the premixed burn spike consists of the combustion of this fuel-rich mixture. The upstream extent of this activity (fuel breakdown and PAH formation) is not certain because the field of view in Figs. 11 and 13 was limited to the region downstream of 27 mm from the injector. Accordingly, the border between the region of PAH or soot and the vapor-fuel/air mixture is shown as gradual fade between colors in the 5.0° and 6.0° ASI schematics.

By 6.0° ASI, soot occurs as very small particles throughout large portions of the cross section of the downstream portion of the fuel jet at locations that vary from cycle to cycle (see Fig. 14). The soot and PAH distributions shown in the 6.0° ASI schematic are representative, but the patterns are not consistent enough to call any particular distribution "typical." These small soot particles that form up throughout the cross section are arising from the fuel-rich premixed burn. By 6.5° ASI, soot is found throughout the cross-section of the downstream region of the jet.

Onset of the Diffusion Flame (5.5° - 6.5° ASI) - Between 5.5° and 6.5° ASI, a diffusion flame forms at the jet periphery between the products of the fuel-rich premixed burn (which contain a significant quantity of unconsumed fuel) and the surrounding air (see Fig. 16). By 6.5° ASI (just prior to the midpoint of the premixed burn spike in the apparent heat release rate), this thin diffusion flame completely encircles the downstream portion of the jet as indicated by the orange color in the schematic. It extends back toward the injector to a point just upstream of the tip of the liquid fuel penetration. As depicted in the schematic, the liquid-fuel length becomes about 2 to 3 mm shorter as the diffusion flame forms, presumably due to local heating by the flame. Also at 6.5° ASI, the soot particles become larger in a thin layer around the jet periphery (not shown in the schematic), due to some effect of the diffusion flame. However, it is important to note that there is no indication of a corresponding increase in soot concentration (volume fraction) at the jet periphery with the formation of the diffusion flame.

Last Part of Premixed Burn Spike (7.0° - 9.0° ASI) - Through the remainder of the premixed burn, the jet continues to grow and penetrate across the chamber. The soot concentration continues to increase throughout the cross section of the sooting region, with the greatest increase in concentration being toward the leading edge where the head vortex is forming. This high soot concentration is indicated in the 8.0° ASI schematic by the red zone near the leading edge. The diffusion flame remains as a thin reaction zone at the jet periphery, and the larger soot particles produced by this flame become distributed inward from the periphery for a few millimeters (not shown), presumably due to turbulent mixing. However, they do not spread into the central region of the jet which is filled only with small soot particles. Although the soot particles all around the jet periphery are larger than those in the central region, the particles toward the leading edge (head-vortex region) are even larger than those along the sides of the jet. Thus, a region of even larger soot particles starts to form near the leading edge with a distribution similar to the red, high-soot-concentration region shown in the 8.0° ASI schematic (see Figs. 14 and 15a).

Toward the end of the premixed burn as the last of the premixed air is consumed, the small soot particles present throughout the cross section extend upstream to approximately 27 mm from the injector. Going from the vapor-fuel region downstream, the soot particles appear rather abruptly across the entire cross section of the jet at this 27 mm location as shown in the 8.0° ASI schematic. No soot can be seen closer to the injector with the low-sooting fuel. However,

some data using the reference fuel indicate that there may be a thin soot zone at the periphery of the jet (just inside of the diffusion flame) in the region between the tip of the liquid fuel and the main soot zone. In the 8.0° ASI schematic, this is indicated by the thin dark blue zone along the side of the diffusion flame in this region. This region will be discussed in greater detail in the next subsection under the Uncertainties and Expected Features sub-subheading.

First Part of the Mixing-Controlled Burn (9.0° ASI to end of injection) - As the combustion transitions to being purely mixing-controlled, the overall appearance of the jet shows only moderate changes. This is probably because the jet was already almost in a mixing-controlled-burn mode as the last of the premixed fuel was burning out. As shown in the 10° ASI schematic, the jet has penetrated further, and the head vortex is becoming well formed. In addition, the soot concentration is higher throughout the head vortex (as indicated by the red and yellow colors), and the soot particles in the head vortex have grown much larger (not shown, see Fig. 15a). However, the soot still appears quite abruptly across the entire cross section of the jet about 27 mm downstream of the injector, as evident in the 9.0° and 11.0° ASI images in Fig. 15a. These soot particles are small when they first appear at the upstream edge of the sooting region, and they remain small throughout the central part of the jet, except for the head vortex region. The data also suggest that soot particles caused by the diffusion flame, that are larger than those in the central part of the jet but smaller than those in the head vortex, are still present along the sides of the jet upstream of the head vortex, like they were during the latter part of the premixed burn.

The same overall jet appearance and soot distribution pattern continue up through the end of fuel injection (for the condition studied), although soot concentrations and particle sizes increase in the head vortex region. A schematic showing the appearance of a typical "developed" (or quasi-steady) reacting diesel fuel jet during this first part of the mixing-controlled burn is presented in Fig. 18, and discussed in the following subsection.

MIXING-CONTROLLED COMBUSTION

Conceptual Model - Figure 18 presents a typical schematic of the conceptual model of DI diesel combustion during the mixing-controlled burn, prior to the end of fuel injection. In this article, no attempt is made to extend the conceptual model beyond the end of fuel injection to the latter part of the mixing-controlled burn. This is because the only data are the soot images in Fig. 15b, which are not sufficient for a full description.

Temporally, the schematic in Fig. 18 follows the last one in the sequence (10° ASI) in Fig. 17, and it is representative of the remainder of the mixing-controlled burn up until the end of injection. Figure 18 is drawn at a somewhat smaller scale than Fig. 17; however, the size is only "representative," since a real jet grows across this time period. This typical schematic is similar in appearance to the 10° ASI schematic in Fig. 17 except that the jet is somewhat larger, and the soot concentration in the head vortex is higher. The soot particles in the head vortex have also grown even larger although this is not shown in the schematic. In addition, the jet boundaries in Fig. 18 have been drawn with a ragged appearance to suggest the turbulent nature of a real diesel jet.

Going from the injector down the jet, Fig. 18 shows that turbulent air entrainment is sufficient to vaporize all the fuel by the time it has traveled about 18 or 19 mm from the injector (for this operating condition). A short distance downstream of this point, the vapor fuel and entrained air have formed a relatively uniform mixture (as indicated by fuel/air mixture measurements at 27 mm for a non-reacting jet and prior to the start of combustion, shown in Fig. 11). Then, at about 27 mm from the injector, soot appears as small particles across the entire cross section of the jet. The soot concentration and particle size increase down the jet to the head vortex, with the highest soot concentrations and largest soot particles occurring in the head vortex. This soot distribution pattern, combined with the flow patterns in a penetrating jet, suggests that soot formation starts at the 27 mm location, and that formation and particle growth continue as the soot moves down the jet to the head vortex. The soot particles then accumulate in the recirculating head vortex where they have time to grow to a very large size. In addition, some of the soot particles eventually reach the diffusion flame at the periphery of the jet where they can be oxidized by OH radical attack as discussed in the next subsection.

Uncertainties and Expected Features - Although laser-sheet imaging has provided considerable information about DI diesel combustion, some of the processes occurring in the region between the tip of the liquid fuel and the point where soot appears throughout the cross section at about 27 mm are not yet well understood.* Figure 18 depicts what the imaging data have shown, with the exception that the thin layer of soot shown along the inside of the diffusion flame in this region has not been verified. For the low-sooting fuels, neither LII nor soot luminosity images show a signal upstream of about 27 mm where soot appears throughout the jet cross-section (see Fig. 15a). With the reference fuel, high soot concentrations make the jet optically thick and LII could not be applied; however, soot luminosity extends upstream almost to the tip of the liquid-phase fuel [13]. The most likely explanation is that shown in Fig. 18. A very thin layer of soot forms along the diffusion flame upstream of the main soot-formation region, one that is too thin both physically and optically to be detected when the low-sooting fuel is used. However, with the much higher soot concentrations produced by the reference fuel, this physically thin zone would not be optically thin, and the soot luminosity would be detectable. The presence of this thin soot layer would also be expected because local heating by the diffusion flame would promote fuel pyrolysis and soot formation upstream of the location where soot forms across the central part of the jet.

* The discussion of these uncertainties applies to the mixing-controlled burn up until the end of injection (Fig. 18), and to the last part of the premixed burn (8.0° and 10.0° ASI schematics Fig. 17).

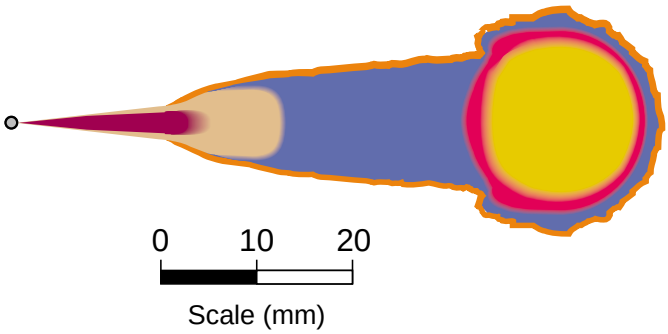

Figure 18. A schematic showing the conceptual model of DI diesel combustion derived from laser-sheet imaging for a typical time during the first part of the mixing controlled burn (*i.e.* prior to the end of injection). The color coding is the same as that given in Fig. 17.

The other main uncertainty is the cause of the initial soot formation across the entire jet cross-section at about 27 mm. It cannot result from fuel pyrolysis induced only by the hot (1000 K) in-cylinder air since soot formation typically requires temperatures above 1300 K [39]. Nor is heating of the jet core by the transport of hot products from the diffusion flame inward a plausible mechanism, since this would produce a progressive inward growth of the thin sooting zone along the diffusion flame in the region upstream of 27 mm (discussed above). This would conflict with the soot images which show no indication of such a progressive growth.

As shown schematically in Fig. 19 (light blue color) and discussed in Ref. [14], a standing fuel-rich premixed flame, just upstream of where the soot first appears, seems to be the most likely alternative. This is in agreement with the data in Fig. 11 which show that prior to combustion (and at later times for the non-reacting jet) the fuel and air are well mixed to a fuel-rich but combustible mixture (equivalence ratio of 2 to 4) just downstream of the maximum liquid penetration. Although in Figs. 18 and 19, the amount of air entrainment would be lower due to the shorter liquid length and presence of the diffusion flame, a significant quantity of air would still be mixed with the fuel by the time the last liquid has vaporized. This nearly uniform, fuel-rich mixture (perhaps an equivalence ratio of 3 to 5) would support a standing premixed flame or reaction zone across the jet just upstream of where the soot appears.* A fuel-rich flame of this type would create an almost ideal environment for soot production because the products contain an abundance of excess fuel and are sufficiently hot for fuel pyrolysis and soot formation. This explanation is also supported by the soot particle-size distribution which shows the upstream and central region of the jet containing only very small soot particles similar to those produced by the initial premixed burn. No evidence of the larger soot particles associated with the diffusion flame is seen in the central part of the jet.

The presence of this standing premixed flame throughout the mixing controlled burn, combined with the description of the premixed-burn-spike combustion shown in Fig. 17, would mean that all of the fuel (both for the premixed and mixing-controlled burn) first undergoes fuel-rich premixed combustion and later diffusion-flame combustion. Furthermore, the diffusion-flame combustion would occur as a flame between the products of the fuel-rich premixed combustion and air rather than being a more classical pure-fuel/air diffusion flame.

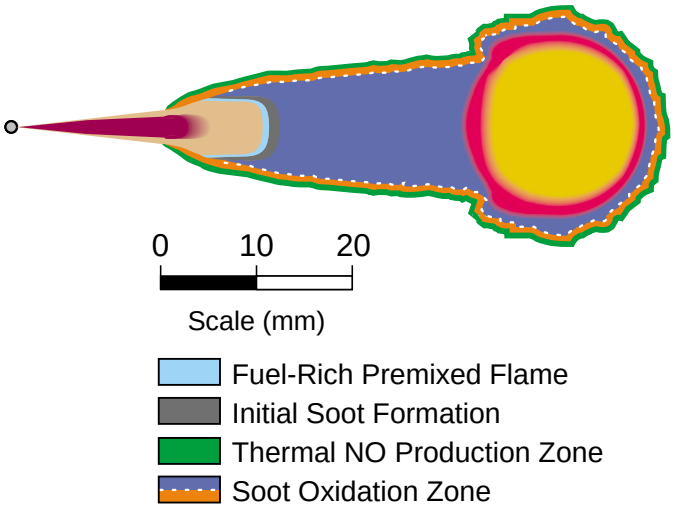

Figure 19. A schematic of the conceptual model from Fig. 18 with additional features (fuel-rich premixed flame, soot formation, soot oxidation, and NO formation zones) that are indicated by the data but have not yet been verified. The color coding is the same as Figs. 17 and 18 except for the additional colors given in the legend at the bottom.

RAMIFICATIONS FOR SOOT AND NO_X PRODUCTION

In addition to the premixed combustion zone discussed above, Fig. 19 shows the expected regions of soot formation, soot oxidation and NO production during the first part of the mixing controlled burn. As shown by the gray zone in the figure, the initial soot formation is thought to occur just downstream of the hypothesized standing fuel-rich premixed flame in the products of the rich combustion. By the time these rich-combustion products reach about 27 mm, small soot particles form throughout the mixture. Then, as discussed above, soot formation and particle growth continue as the soot moves down the jet to the head vortex and/or outward to the diffusion flame. The diffusion flame is the only source of high OH radical concentrations (see Fig. 16), and OH radical attack is thought to be the primary method of soot oxidation, as discussed in Ref. [14]. Oxygen attack may also play a role, but the diffusion flame is also the only location where oxygen would be expected. As a result, soot oxidation is almost certainly occurring at the diffusion flame throughout this portion of the combustion event. This is indicated by the dashed white line in Fig. 19.

* This mixture is probably beyond the rich flammability limit for an atmospheric flame with room-temperature reactants; however, for diesel conditions, the fuel-air mixture is hot (700 to 750 K [31]), and the reactants have undergone an induction time almost sufficient to bring them to autoignition prior to reaching this standing fuel-rich flame zone. This standing premixed flame is thought to be established during the later stages of the initial premixed burn, from about 6.0° to 8.0° ASI as the fuel-rich mixture flows into the zone undergoing the initial premixed burn.

The conceptual model of diesel combustion presented above in Figs. 17 and 18 shows that for typical diesel conditions virtually all of the premixed combustion is fuel rich, in the range of an equivalence ratio of 4. This includes both the initial premixed burn just after autoignition and the hypothesized standing premixed flame during the mixing controlled burn. These conditions are not conducive to NO production either by the "thermal" or "prompt" mechanisms. Little oxygen is present and adiabatic flame temperatures (~1600 K) are far below those required for significant thermal NO production. For prompt NO, calculations and experiments show little NO produced at equivalence ratios above 1.8 [58, 59]. However, HCN production might still occur in this rich combustion [59], and if it does, it is likely that the "fixed nitrogen" would later be released as NO at the diffusion flame [58, 59].

Subsequent to this fuel-rich premixed combustion, the remaining fuel burns as a diffusion flame at the jet periphery. At the diffusion flame temperatures will be high (combustion is nearly stoichiometric), and there is a source of oxygen. These conditions are nearly ideal for thermal NO production. Accordingly, for the time period depicted by the conceptual model (*i.e.* up through the end of fuel injection) high NO production rates by the thermal mechanism are expected only around the jet periphery on the lean side of the diffusion flame, as indicated by the green line in Fig. 19.

However, it is important to realize that the NO-production zone shown in Fig. 19 may not be the location where most of the NO is produced during typical diesel combustion. Thermal NO production is a relatively slow process, and this could delay the onset of significant NO production until after the time period represented by Figs. 17 to 19. Hence, the bulk of the NO production might occur during the latter part of the mixing controlled burn or in hot-gas regions that remain after the end of combustion (time periods not depicted in the current conceptual model). Although peak temperatures may be lower in these regions than they are at the diffusion flame prior to the end of injection, there is considerably more time for the NO-production reactions, and the volume of gas involved could be much larger.

In addition, some NO may be produced at the diffusion flame by the "prompt" mechanism and by conversion of "fixed nitrogen" from the rich premixed combustion. However, for combustion at diesel temperatures these mechanisms are expected to be less important than the thermal mechanism.

COMPARISON OF THE OLD DESCRIPTION AND NEW CONCEPTUAL MODEL

The schematics shown on the previous pages show that both the premixed and mixing-controlled combustion phases of diesel combustion occur differently from what had been thought prior to the recent laser imaging data. As mentioned in the Introduction and Background sections, autoignition and the premixed burn were thought to occur in regions that were nearly stoichiometric, primarily around the jet periphery [7]. In addition, ignition was thought to occur at only a few points followed by a rapid spread of the flame around the jet periphery [7]. The data presented here show a very different picture. As discussed above, chemiluminescence imaging shows ignition occurring progressively at multiple points across the downstream regions of all the fuel jets, beginning well before the start of the premixed burn spike. The imaging data also show that the vast majority of combustion during the premixed burn spike occurs under fuel-rich conditions (equivalence ratios of 2-4), and that this premixed combustion leads to the initial soot formation.

Similarly, for the mixing-controlled burn (through the end of fuel injection), Figs. 18 and 19 show quite a different picture from the old description in Fig. 5. In contrast with the old description, the actual liquid-fuel penetration length is relatively short, and all the fuel in the main combustion zone is vapor phase. Soot occurs throughout the jet cross-section, rather than only in a shell near the diffusion flame around the jet periphery. The soot first appears just downstream of the liquid-fuel region and grows in size and volume fraction as it flows downstream, eventually being oxidized at the diffusion flame. Finally, although the diffusion flame does appear only around the jet periphery as previously thought, there is evidence that throughout the mixing-controlled burn, the fuel undergoes rich premixed combustion prior to reaching the diffusion flame.

Despite the seemingly large differences between the old and new schematics of DI diesel combustion, most of the fundamental arguments made by the developers of the spray combustion theory upon which Fig. 5 is based (*e.g.* Faeth [2] and H. Chiu and co-workers [4, 37]) appear to be correct. The differences arise mainly from three characteristics of modern diesel combustion that may not have been fully appreciated. First, injection velocities are very high which causes the flame to stand off from the injector allowing significant air entrainment upstream of the diffusion-flame zone. This entrainment of hot in-cylinder air promotes rapid vaporization of the liquid fuel and results in a rich but combustible mixture downstream of the liquid. Second, mixing rates upstream of the tip of the liquid penetration must be very high, since the vapor-fuel and air have formed a "relatively uniform" mixture just downstream of this point. Third, for turbulent jets the instantaneous picture can be very different from a statistically averaged picture. Much of the data upon which early spray theory was based came from time-averaged measurements which typically give a Gaussian distribution across a turbulent jet, as shown in Fig. 1. However, the instantaneous picture can be quite different with very steep gradients, as shown in many of the images presented here. For example, if vapor fuel images like those in Fig. 11 from many engine cycles are averaged together, the resulting distribution of equivalence ratio looks quite Gaussian from the center of the jet to the edge; however, as the typical images in Fig. 11 show, this is not the case for any single instantaneous image.

It is also noteworthy that the picture of diesel combustion described in this article shows a relatively well organized process. Events happen in a logical sequence as the fuel travels down the jet, undergoing the various steps in the process that we call diesel combustion. In addition, mixing rates

appear to be sufficiently high that many parts of the jet are relatively homogeneous and well characterized. The picture that has emerged is very different from the "holocaust where nothing is homogeneous" postulated by W. G. Agnew in 1984 [1], as discussed in the Background section. However, it should be noted that Agnew recognized the lack of understanding of diesel combustion and advocated additional research of the kind reported here. The new, relatively well organized picture of diesel combustion also helps explain the apparent paradox noted by Agnew that despite the stochastic nature of diesel combustion, "the overall heat-release process is much more repeatable than in gasoline engines."

SUMMARY AND CONCLUDING REMARKS

Over the past eight years, a wide variety of laser-sheet-imaging and other optical diagnostics have been applied to DI diesel combustion by the author and co-workers, and others. These investigations have added considerably to our understanding of diesel combustion, but they have generally focused on the details of one or two particular aspects of the process. In this article, results from these past investigations have been combined with additional original data, to form a phenomenological description or "conceptual model" of how DI diesel combustion occurs in the absence of swirl or wall interactions.

To provide the background for the conceptual model, selected images and image sequences from past investigations of the author and co-workers were reviewed including: liquid- and vapor-phase fuel distributions, quantitative vapor-fuel/air mixture images, relative soot concentration and particle-size distributions, images of the diffusion flame structure, and natural chemiluminescence and soot-luminosity images. Original data were also presented, including PAH distributions and soot distributions throughout the mixing controlled burn for a relatively high-load condition. In addition, the results of these individual studies were related to one another, and discussed with respect to other supporting data from the literature, to form a more complete picture of the diesel combustion process.

This new picture of DI diesel combustion was then presented in a series of idealized schematics depicting the combustion process for a typical modern-diesel-engine condition. These schematics incorporate all of the information from the imaging studies mentioned above and show the temporal evolution of a reacting diesel fuel jet from the start of fuel injection up through the first part of the mixing-controlled burn (until the end of fuel injection). In addition, for a "developed" reacting fuel jet during the mixing-controlled burn, the schematics explain the sequence of events that occurs as fuel moves from the injector downstream through the mixing, combustion, and emissions-formation processes. Finally, the implications of this new understanding of diesel combustion on the mechanisms of soot formation, soot destruction, and NO formation have been summarized and discussed. The conceptual model of DI diesel combustion depicted in these schematics differs significantly from what had been thought prior to the laser-sheet imaging investigations.

Although the conceptual model of diesel combustion presented in these schematics is fairly complete for the portion of the diesel combustion event depicted, improvement or expansion of the model is needed in four main areas. First, uncertainties exist about some aspects, particularly in the region between the tip of liquid fuel and the point where soot appears throughout the cross section. The hypothesized standing fuel-rich premixed flame and thin soot layer along the diffusion flame need to be verified or disproved. Second, the model needs to be extended to cover the burnout phase of diesel combustion (*i.e.* the latter part of the mixing controlled burn from the end of fuel injection to the end of combustion). Third, the model is currently based on detailed imaging data taken primarily at one typical operating condition with idealized fuels. Parameters such as TDC temperature and density [27, 29], injector hole size [48], injection pressure [47], and fuel properties [48] are known to affect either the temporal and/or spatial scaling of various components within the reacting fuel jet. Additional data and scaling laws (similar to those for overall jet penetration, *e.g.* [27]) are needed to extend the conceptual model beyond the typical operation condition shown in the schematics, and to include the effects of real fuels. Fourth, the effects of wall interactions and swirl need further investigation.

Despite these limitations, the conceptual model of DI diesel combustion presented here correlates virtually all of the data from a wide variety of imaging diagnostics, and it unifies these data into a description of how DI diesel combustion occurs for a typical modern-diesel-engine condition.

ACKNOWLEDGMENTS

The author would like to thank Christoph Espey (now with Mercedes-Benz) and Dennis Siebers, both of whom have provided valuable feedback during of the development of the ideas presented in this article. In addition, Christoph Espey has been a co-author on many of the supporting papers. I am also grateful to Eldon Porter for maintaining the experimental apparatus and for help with the data acquisition. The author would also like to express his gratitude to Patrick Flynn and Roy Primus of the Cummins Engine Co. for their continual strong support of this project.

This work was performed at the Combustion Research Facility, Sandia National Laboratories, Livermore, CA. The author thanks the U.S. Department of Energy, Defense Programs Technology Transfer Initiative and the Office of Transportation Technologies, and the Cummins Engine Company for supporting this work.

REFERENCES

1. Agnew, W. G., "Room at the Piston Top: Contributions of Combustion Science to Engine Design," *Twentieth Symposium (International) on Combustion*, pp. 1-17, 1984.
2. Faeth, G. M., "Current Status of Droplet and Liquid Combustion," *Prog. Energy Combust. Sci.*, Vol. 3, pp. 191-224, 1977.

3. Kuo, K. K., Principles of Combustion, Wiley & Sons, New York, pp. 589-594, 1986
4. Chiu, H. H., Kim, H. Y., and Croke, E. J., "Internal Group Combustion of Liquid Droplets," *Nineteenth Symposium (International) on Combustion*, pp. 971-980, 1982.
5. Chiu, W. S., Shahed, S. M., and Lyn, W. T., "A Transient Spray Mixing Model for Diesel Combustion," *SAE Transactions*, Vol. 85, pp. 502-512, paper no. 760128, 1976.
6. Rife, J. and Heywood, J. B., "Photographic and Performance Studies of diesel Combustion with a Rapid Compression Machine," *SAE Transactions*, Vol. 83 pp. 2942-2961, paper no. 740948, 1974.
7. Heywood, J. B., Internal Combustion Engine Fundamentals, McGraw-Hill, New York, 1988.
8. Bosch Automotive Handbook, 3rd Ed., Robert Bosch GmbH, Stuttgart, Germany, worldwide distribution through the SAE, Warrendale, PA, 1993.
9. Bardsley, M. E. A., Felton, P. G., and Bracco, F. V., "2-D Visualization of Liquid and Vapor Fuel in an I.C. Engine," *SAE Transactions*, Vol. 97, Sec. 3, pp. 3.281-3.291, paper no. 880521, 1988.
10. Heinze, T. and Schmidt, T., "Fuel-Air Ratios in a Spray, Determined between Injection and Autoignition by Pulsed Spontaneous Raman Spectroscopy," *SAE Transactions*, Vol. 98, Sec. 3, pp. 2088-2094, paper no. 892102, 1989.
11. zur Loye, A. O., Siebers, D. L., and Dec, J. E., "2-D Soot Imaging in a Direct-Injection Diesel Engine Using Laser-Induced Incandescence," Proceedings of the International Symposium on Diagnostics and Modeling of Combustion in Internal Combustion Engines, COMODIA 90, pp. 523-528, 1990.
12. Dec, J. E., zur Loye, A. O., and Siebers, D. L., "Soot Distribution in a D.I. Diesel Engine Using 2-D Laser-Induced Incandescence Imaging," *SAE Transactions*, Vol. 100, Sec. 3, pp. 277-288, paper no. 910224, 1991.
13. Espey, C. and Dec, J. E., "Diesel Engine Combustion Studies in a Newly Designed Optical-Access Engine Using High-Speed Visualization and 2-D Laser Imaging," *SAE Transactions*, Vol. 102, Sec. 4, pp. 703-723, paper no. 930971, 1993.
14. Dec, J. E. and Coy, E. B., "OH Radical Imaging in a DI Diesel Engine and the Structure of the Early Diffusion Flame," SAE paper no. 960831, 1996.
15. Lee, W., Solbrig, C. E., Litzinger, T. A., Santoro, R. J., and Santavicca, D. A., "Planar Laser Light Scattering for the In-Cylinder Study of Soot in a Diesel Engine," *SAE Transactions*, Vol. 99, Sec. 3, pp. 2222-2235, paper no. 902125, 1990.
16. Alatas, B., Pinson, J. A., Litzinger, T. A., and Santavicca, D. A., "A Study of NO and Soot Evolution in a DI Diesel Engine via Planar Imaging," *SAE Transactions*, Vol. 102, Sec. 3, pp. 1463-1473, paper no. 930973, 1993.
17. Pinson, J. A., Ni, T., and Litzinger, T. A., "Quantitative Imaging Study of the Effects of Intake Air Temperature on Soot Evolution in an Optically Accessible D.I. Diesel Engine," SAE paper no. 942044, 1994.
18. Hodges, J. T., Baritaud, T. A., and Heinze, T. A., "Planar Liquid and Gas Fuel and Droplet size Visualization in a DI Diesel Engine," *SAE Transactions*, Vol. 100, Sec. 3, pp. 1284-1302, paper no. 910726, 1991.
19. Baritaud, T. A., Heinze, T. A., and Le Coz J. F., "Spray and Self-Ignition Visualization in a DI Diesel Engine," *SAE Transactions*, Vol. 103, Sec. 3, pp. 1129-1144, paper no. 940681, 1994.
20. Arnold, A., Dinkelacker, F., Heitzmann, T., Monkhouse, P., Schäfer, M., Sick, V. and Wolfrum, J., "DI Diesel Engine Combustion Visualized by Combined Laser Techniques," *Twenty-Fourth Symposium (International) on Combustion*, pp. 1605-1612, 1992.
21. Won, Y.-H., Kamimoto, T., Kobayashi, H., and Kosaka, H, "2-D Soot Visualization in Unsteady Spray Flame by means of Laser Sheet Scattering Technique," *SAE Transactions*, Vol. 100, Sec. 3, pp. 265-276, paper no. 910223, 1991.
22. Kosaka, H., Nishigaki, T., and Kamimoto, T., "A Study on Soot Formation and Oxidation in an Unsteady Spray Flame via Laser-Induced Incandescence and Scattering Techniques," *SAE Transactions*, Vol. 104, Sec. 4, pp. 1390-1399, paper no. 952451, 1995.
23. Kosaka, H., Nishigaki, T., Kamimoto, T., Sano, T., Matsutani, A. and Harada, S., "Simultaneous 2-D Imaging of OH Radicals and Soot in a Diesel Flame by Laser Sheet Techniques," SAE paper no. 960834, 1996.
24. Ragucci, R., Cavaliere, A. and D'Alessio, A., "Laser Assisted Diagnostics for Characterization of Condensed Phases During Diesel Combustion Processes," Proceedings of the International Symposium on Diagnostics and Modeling of Combustion in Internal Combustion Engines, COMODIA 90, pp. 371-376, 1990.
25. Suzuki, M. Nishida, K. and Hiroyasu, H., "Simultaneous Concentration Measurement of Vapor and Liquid in an Evaporating Diesel Spray," *SAE Transactions*, Vol. 102, Sec. 3, pp. 1164-1186, paper no. 930863, 1993.
26. Megahed, M., "First Measurements of the Liquid-Phase Temperature in Diesel Sprays," SAE paper no. 930969, 1993.
27. Naber, J. D. and Siebers, D. L., "Effects of Gas Density and Vaporization on Penetration and Dispersion of Diesel Sprays," SAE paper 960034, 1996.
28. Wiltafsky, G., Stolz, W., Köhler, J., and Espey C., "The Quantification of Laser-Induced Incandescence (LII) for Planar Time Resolved Measurements of the Soot Volume Fraction in a Combustion Diesel Jet," SAE paper 961200, 1996.
29. Espey, C. and Dec, J. E., "The Effect of TDC Temperature and Density on the Liquid-Phase Fuel Penetration in a D.I. Diesel Engine," *SAE Transactions*, Vol. 104, Sec. 4, pp. 1400-1414, paper no. 952456, 1995.

30. Espey, C., Dec, J. E., Litzinger, T. A. and Santavicca, D. A., "Quantitative 2-D Fuel Vapor Concentration Imaging in a Firing D.I. Diesel Engine Using Planar Laser-Induced Rayleigh Scattering," *SAE Transactions*, Vol. 103, Sec. 3, pp. 1145-1160, paper no. 940682, 1994.
31. Espey, C., Dec, J. E., Litzinger, T. A. and Santavicca, D. A., "Planar Laser Rayleigh Scattering for Quantitative Vapor-Fuel Imaging in a Diesel Jet," *Combustion and Flame*, in press 1997.
32. Dec, J. E. and Espey, C., "Soot and Fuel Distributions in a D.I. Diesel Engine via 2-D Imaging," *SAE Transactions*, Vol. 101, Sec. 4, pp. 1642-1651, paper no. 922307, 1992.
33. Dec, J. E., "Soot Distribution in a D.I. Diesel Engine Using 2-D Imaging of Laser-Induced Incandescence, Elastic Scattering, and Flame Luminosity," *SAE Transactions*, Vol. 101, Sec. 4, pp. 101-112, paper no. 920115, 1992.
34. Dec, J. E. and Espey, C., "Ignition and Early Soot Formation in a D.I. Diesel Engine Using Multiple 2-D Imaging Diagnostics," *SAE Transactions*, Vol. 104, Sec. 3, pp. 853-875, paper no. 950456, 1995.
35. Dec, J. E. and Espey, C. "Soot and Liquid-Phase Fuel Distributions in a Newly Designed Optically Accessible D.I. Diesel Engine," Proceedings of the 1993 Diesel Emission Reduction Workshop, La Jolla, CA, July 1993, and Sandia National Laboratories Report No. SAND93-8690C.
36. Sichel, M. and Palaniswamy, S., "Sheath Combustion of Sprays," *Twentieth Symposium (International) on Combustion*, pp. 1789-1798, 1984.
37. Chiu, H. H. and Croke, E. J., "Group Combustion of Liquid Fuel Sprays," Energy Technology Lab Report 81-2, Univ. of Illinois at Chicago, 1981.
38. Greeves, G., Khan, I. M., Wang, C. H. T., and Fenne, I. "Origins of Hydrocarbon Emissions from Diesel Engines, *SAE Transactions*, Vol. 86, Sec. 2, pp. 1235-1251, paper no. 770259, 1977.
39. Wagner, H. Gg., "Soot Formation - An Overview," pp. 1-29, Particulate Carbon Formation During Combustion, D.C. Siegla and G.W. Smith editors, Plenum, Press, New York, 1981.
40. Kamimoto, T. and Kobayashi, H. "Combustion Processes in Diesel Engines," *Prog. Energy Combust. Sci.*, Vol. 17, pp. 163-189, 1991.
41. Kamimoto, T. and Bae, M-H., "High Combustion Temperature for the Reduction of Particulate in Diesel Engines," *SAE Transactions*, Vol. 97, pp. 6.692-6.701, paper no. 880423, 1988.
42. Melton, L. A., "Soot Diagnostics Based on Laser Heating," *Applied Optics*, Vol. 23, No. 13, pp. 2201-2208, 1984.
43. Quay, B., Lee, T., Ni, T., and Santoro, R. J., "Spatially Resolved Measurements of Soot Volume Fraction Using Laser-Induced Incandescence," *Combustion and Flame*, Vol. 97, pp. 384-392, 1994.
44. Pinson, J. A., Mitchell, D. L., Santoro, R. J., and Litzinger, T. A., "Quantitative, Planar Soot Measurements in a D.I. Diesel Engine Using Laser-Induced Incandescence and Light Scattering," SAE paper no. 932650, 1993.
45. Kerker, M., The Scattering of Light and Other Electromagnetic Radiation, Academic Press, San Diego, 1969.
46. zur Loye, A. O., Siebers, D. L., McKinley, T. L., Ng, H. K., and Primus, R. J., "Cycle-Resolved LDV Measurements in a Motored Diesel Engine and Comparison with k-ε Model Predictions," *SAE Transactions*, Vol. 98, Sec. 3, pp. 1142-1158, paper no. 890618, 1989.
47. Kamimoto, T., Yokota, H., and Kobayashi, H., "Effect of High Pressure Injection on Soot Formation Processes in a Rapid Compression Machine to Simulate Diesel Flames," *SAE Transactions*, Vol. 96, Sec. 4, pp. 4.783-4.791, paper no. 871610, 1987.
48. Browne, K. R., Partridge, I. M., and Greeves, G., "Fuel Property Effects on Fuel/Air Mixing in an Experimental Diesel Engine," SAE paper 860223, 1986.
49. Bower, G. R. and Foster D. E., "The Effect of Split Injection of Fuel Distribution in an Engine-Fed Combustion Chamber," *SAE Transactions*, Vol. 102, Sec. 3, pp. 1187-1202, paper no. 930864, 1993.
50. Personal Communication with Dennis L. Siebers, Sandia National Laboratories, 1996.
51. Henein, N. A., "Analysis of Pollutant Formation and Control and Fuel Economy in Diesel Engines," *Prog. Energy Combust. Sci.*, Vol. 1, pp. 165-207, 1976.
52. Edwards, C. F., Siebers, D. L., and Hoskin, D. H, "A Study of the Autoignition Process of a Diesel Spray via High Speed Visualization," *SAE Transactions*, Vol. 101, Sec. 3, pp. 187-204, paper no. 920108, 1992.
53. Keller, J. O. and Westbrook, C. W., "Response of a Pulse Combustor to Changes in Fuel Composition," Twenty-First Symposium (International) on Combustion, pp. 547-555, 1986.
54. Gaydon, A. G., The Spectroscopy of Flames, Chapman and Hall Ltd., London, 1974.
55. Crosley, D. R. and Dyer, M. J., "Two-Dimensional Imaging of Laser-Induced Fluorescence in OH in a Flame," Proceedings of the International Conference on Lasers, Dec. 1982.
56. Berlman, I. B., Handbook of Fluorescence Spectra of Aromatic Molecules, Academic Press, 1971.
57. Paul, P. H. and Dec, J. E., "Imaging of Reactions Zones in Hydrocarbon-Air Flames using Planar Laser-Induced Fluorescence of CH," *Optics Letters*, Vol. 19, No. 13, pp. 998-1000, 1994.
58. Glarborg, P., Miller, J. A., and Kee, R. J. "Kinetic Modeling and Sensitivity Analysis of Nitrogen Oxide Formation in Well-Stirred Reactors," *Combustion and Flame*, Vol. 65, pp. 177-202, 1986.
59. Miller, J. A. and Bowman, C. T., "Mechanism and Modeling of Nitrogen Chemistry in Combustion," *Prog. Energy Combust. Sci.*, Vol. 15, pp. 287-338, 1989.